International Journal of Plasticity 172 (2024) 103863

Contents lists available at ScienceDirect

International Journal of Plasticity

journal homepage: www.elsevier.com/locate/ijplas

A dislocation-density-based crystal plasticity model for FCC nanocrystalline metals incorporating thermally-activated depinning from grain boundaries

Jonathan Cappola [a,c], Jian Wang [b], Lin Li [a,c,*]

[a] School for Engineering of Matter, Transport and Energy, Arizona State University, Tempe, AZ 85287, United States of America
[b] Mechanical and Materials Engineering, University of Nebraska-Lincoln, Lincoln, NE 68588, United States of America
[c] Department of Metallurgical and Materials Engineering, The University of Alabama, Tuscaloosa, AL 35487, United States of America

ARTICLE INFO

Keywords:
Nanocrystalline metals
Thermally activated process
Dislocations
Crystal plasticity
Finite elements

ABSTRACT

A novel dislocation-density-based crystal plasticity model for nanocrystalline face-centered cubic metals is developed based on the thermally-activated mechanism of dislocations depinning from grain boundaries. Dislocations nucleated from grain boundary dislocation sources are assumed to be the primary carriers of plasticity in the nanocrystals. The evolution of the dislocation density thereby involves a competition between the nucleation of dislocations from grain boundary defect structures, such as ledges, and the absorption of dislocations into the grain boundary via diffusion processes. This model facilitates the simulation of plastic deformation in nanocrystalline metals, with consideration of the initial microstructure resulting from a particular processing method, to be computed as a direct result of dislocation-mediated plasticity only. The exclusion of grain boundary-mediated plasticity mechanisms in the formulation of the crystal plasticity model allows for the exploration of the fundamental role dislocations play in nanocrystalline plasticity. The combined effect of average grain size, grain size distribution shape, and initial dislocation density on the mechanical performance and strain-rate sensitivity are explored with the model. Further, the influence of the grain boundary diffusivity on post-yielding strain-hardening behavior is investigated to discern the impact that the choice of processing route has on the resulting deformation response of the material.

1. Introduction

For face-centered cubic (FCC) metals, the reduction of the grain size into the nanocrystalline (NC) regime results in deviation from deformation mechanisms typical of coarse-grained metals as the grain boundaries (GBs) become increasingly active in plasticity (Meyers et al., 2006). The accommodation of plastic deformation through the GBs in nanocrystals can occur either directly, from mechanisms such as sliding (Gifkins, 1976), or indirectly, by acting as both sources and sinks for dislocations (Li et al., 2021). While competition between GB-mediated plasticity and dislocation-mediated plasticity may be expected across the nanometer regime, it has been suggested that dislocations nucleated from GBs play a dominant role in NC plasticity down to several tens of nanometers, below which GB-mediated plasticity may become prevalent (Brink and Albe, 2018). As such, consideration of the interplay between dislocations and GBs is critical in understanding how plasticity develops in NCs, in contrast to their coarse-grained counterparts.

* Corresponding author at: School for Engineering of Matter, Transport and Energy, Arizona State University, Tempe, AZ 85287, United States of America.
E-mail address: lin.li.10@asu.edu (L. Li).

https://doi.org/10.1016/j.ijplas.2023.103863
Received 24 August 2023; Received in revised form 6 December 2023
Available online 22 December 2023

Although the reduced grain size of nanocrystals produces a shift in the preferred nucleation site for dislocations from the grain interior to the boundary, dislocations remain an active carrier of plastic deformation. This has been directly observed, from in-situ tension experiments performed using transmission electron microscopy (TEM), in both ultra-fine-grained (UFG) Al and Au (Chrominski and Lewandowska, 2018; Gupta et al., 2020) highlighting the continued activity of dislocations and their increased interactions with the GBs at this length-scale. The probability of dislocation–dislocation interactions within the grain interior is significantly reduced in nanocrystals, with it being generally accepted that interiors are defect-free in the absence of load (Yamakov et al., 2001). Instead, the lifetime of a single dislocation within a nanograin is understood to follow a rather straightforward "nucleation–propagation–absorption" process (Khan and Liu, 2016). That is, dislocations are nucleated at a GB from a defect structure, propagate through the grain interior while continually interacting with the boundary, and absorb (or annihilate) into the opposing GB by a diffusion mechanism. This is the fundamental process motivating the development of mechanistic models for plastic deformation by dislocation motion in NCs.

As the grain size is reduced into the nanoscale regime, the volume fraction of GBs in a NC metal increase significantly compared to their coarse grain counterparts (Borodin and Mayer, 2017). Due to this, the nucleation of an "embryonic" dislocation loop from a pre-existing defect structure at the GB is expected to be relatively easy, owing to local stress concentrations about the boundary defect (Li et al., 2011). This, consequently, suggests that the propagation of a dislocation, which is governed by a thermally-activated depinning process, is more reasonably expected to be the rate-controlling step in the deformation of NCs (Wang et al., 2006), an inference supported by molecular dynamics (MD) simulations (Turlo and Rupert, 2018). Once nucleated, the embryonic dislocation loop will bow out between two pinning points on the GB until a critical shear stress is reached allowing the dislocation to overcome a short-range thermal barrier imposed by one of the pinning points, whereupon propagation through the nanograin interior (and to the next pinning point) may proceed.

Dislocations in NC grains are generally accepted to not accumulate within the grain interior nor interact with other intragranular dislocations throughout their lifetime (Kato, 2009). Despite this, dislocations have been observed experimentally in NCs using in-situ TEM providing evidence for the propagation process of the dislocations through the grain interior after nucleation and emission. Wu and Ma (2006) suggested that dislocations found accumulated within nanograins are stabilized by forces from other defects, such as the GBs or embryonic dislocation loops. In their work, full dislocations operating in a 24 nm grain size nanocrystal were experimentally observed via postmortem TEM examination after deformation at cryogenic and room temperatures, noting a lack of dislocation storage during room temperature deformation suggesting that a thermally activated process governs dislocation motion in nanocrystals. Youssef et al. (2005) observed individual dislocation motion, pile-up, and trapped dislocations in synthesized NC Cu with a mean grain size of 23 nm using in-situ dynamic straining TEM. Kumar et al. (2003) performed in-situ TEM experiments on electro-deposited (ED) Ni with a 30 nm grain size directly observing dislocation activity including emission and absorption at the GBs, further noting the preservation of crystallinity up to the GB. Recently, Wei et al. (2021, 2022) prepared Ni-SiOC core–shell nanostructures and showed that amorphous ceramic GBs act as strong barriers impeding the formation of localized shear bands and allow for co-deformation of the nanograins while preventing grain coarsening.

The process of dislocation absorption into the GBs of NCs is typically neglected and it is generally assumed that GBs act as ideal sinks due to the observed lack of strain hardening in most nanocrystals (Khan and Liu, 2016). The absorption process at a GB requires diffusive relaxation making it inherently temperature dependent (Zhang et al., 2022). This temperature dependence has been shown in NC FCC metals to influence the strain-hardening rate of the materials (Wang et al., 2004, 2006). Lower temperatures will result in depressed absorption at the boundaries, increasing the dislocation storage rate, whereas at higher temperatures, storage rate and absorption will balance each other leading to the lack of strain-hardening (Wang et al., 2004; Witkin et al., 2005). Bouaziz et al. (2010) proposed an extension to the Kocks–Mecking–Estrin (KME) (Mecking and Kocks, 1981; Estrin and Mecking, 1984) dislocation density evolution law that suggested a critical grain size, for which the characteristic time for nucleation and propagation is equal to that of absorption by diffusive processes, below which the dislocation storage rate significantly decreases. Carlton and Ferreira (2007) presented a model to account for the inverse Hall–Petch effect observed in NCs based on dislocation absorption by GBs, arguing that the probability for statistical absorption of a dislocation by the GB is lowered as the grain size increases as the probability of absorption into the GB was related to the probability of core atoms jumping to the GB. Pan and Rupert (2014) performed MD simulations on Cu bicrystals reporting that the ability for GBs to efficiently absorb the free volume of incoming dislocations governs the ductility of NCs. Malygin (2007b) modified the dislocation kinetics of the KME model to account for increased interactions between the GBs and dislocations in NCs as well as allowing for dislocation annihilation into the GB to occur via both pair annihilation (diffusive climb) and core dissolution (atomic shuffling), although the latter is assumed to be comparatively negligible.

The mechanical performance of NCs, like their coarse-grained counterparts, are notably sensitive to their processing methods (Khan et al., 2008). Multiple processing methods have been found to successfully produce NCs, such as ED (Dalla Torre et al., 2005), ball-milling and consolidation (Khan et al., 2008; Farrokh and Khan, 2009), and high pressure torsion (Zhilyaev and Langdon, 2008). Each processing method imparts a particular deformation texture (Zhu et al., 2006; Lohmiller et al., 2014), dislocation density (Gubicza et al., 2018), and grain/GB structure (Dalla Torre et al., 2005; Bober et al., 2016), which constitute the initial state of the microstructure prior to any subsequent deformation in application. The dislocation density measured in NCs is commonly reported to be on the order of 10^{-4}–10^{-2} nm^{-2} (or 10^{14}–10^{16} m^{-2}) (Li et al., 2009b; Kolonits et al., 2015), or several orders of magnitude higher than what is typical for even well-worked coarse-grained materials of the same constituent elements. NCs that are produced with a high initial dislocation density, particularly via severe plastic deformation (SPD), are inclined to exhibit strain-softening behaviors post-yielding (Haouaoui et al., 2004; Gubicza et al., 2018). As such, in the formulation of a constitutive model

for the deformation of NCs by dislocation-mediated plasticity, it is crucial to consider the contribution of the initial dislocation density on both the yielding and post-yielding behaviors.

Various crystal plasticity models have been developed to model particular aspects of NC deformation mechanisms and explain the observed discrepancies from their coarse-grained counterparts. Early work, such as that of Fu et al. (2004), focused on the development of core and mantle approximations which modeled the grain interior (core) and the GB (mantle) as separate material phases with distinct constitutive responses. Zhu et al. (2005) developed an extended Taylor model of crystal plasticity which incorporated the emission of both perfect and partial dislocations as well as GB sliding, reporting the first order effect of the grain size distribution on the mechanical response and strength of NC Ni. Li et al. (2009a) developed a quantized crystal plasticity (QCP) model motivated by observations of dislocation propagation from MD simulations, incorporating a grain size effect through the magnitude of discrete slip events and a statistical distribution to the critical resolved shear stress, predicting that NCs are prone to localization of plastic strain. Yuan et al. (2015) expanded on the QCP model by establishing a link between the statistical distribution of critical resolved shear stress (CRSS) to a GB dislocation source length distribution, noting that the statistical dispersion of CRSS leads to macroscopic strain hardening in NC Ni. Khan and Liu (2016) implemented a Taylor-type crystal plasticity model based on the thermally-activated dislocation depinning mechanism proposed by Kato (2009), accounting for the interaction of the dislocations and the GBs through the evolution of the dislocation density. There remains a lack of full-field crystal plasticity models specially formulated to account for both the plastic deformation mechanisms specific to NCs, particularly the interactions between dislocations and GBs, and the initial microstructural state (i.e., texture, grain size/shape distribution, dislocation density, and GB structure) that results from processing.

In this study, a crystal plasticity model is developed for NC FCC metals based on the thermally-activated mechanism of dislocations depinning from GBs. The proposed model incorporates microstructural information, particularly grain size distribution and initial dislocation density, that arises from a particular production method or processing route. Further, the model is formulated under the constraint that GB-mediated deformation mechanisms are inactive to better examine the contribution of dislocation-mediated plasticity across the nanoscale regime, independent from the influence of other competing deformation mechanisms. It is found that the average grain size, its associated distribution shape, the initial dislocation density magnitude, and the GB diffusivity, all have significant impact on mechanical performance, particularly regarding the yield strength and work-hardening behavior of the simulated NC Cu. In the absence of GB-mediated plasticity mechanisms, it is found that strain-rate sensitivity has a positive correlation with grain size, which is not observed experimentally in NC Cu due to the increasing dominance of GB-mediated plasticity mechanisms as the grain size decreases to less than 10 nm. This study highlights the sensitivity of the mechanical performance of NCs to the microstructural state prior to deformation, provides insight into the role of dislocation-mediated plasticity in nanostructured materials, and identifies the functional limits where dislocation-mediated plasticity in NC Cu is no longer expected to dominate the deformation.

2. Constitutive model formulation

In this section, we summarize the constitutive framework of rate-dependent crystal plasticity for sake of completeness. Following this, expressions for the CRSS, plastic shearing rate, and dislocation density evolution, are constructed on the physical assumptions of dislocation-mediated plasticity in NCs discussed in Section 1. Our proposed constitutive model formulation is then closed through the assumption of a homogeneous plastic response at the grain-level, along with its associated kinematic modifications.

2.1. Framework of rate-dependent crystal plasticity

The kinematic basis for a crystal plasticity constitutive model for finite deformation is the assumption that the total deformation gradient, $\mathbf{F}$, can be multiplicatively decomposed into elastic and plastic components as

$$\mathbf{F} = \mathbf{F}^{\mathrm{e}}\mathbf{F}^{\mathrm{p}}, \tag{1}$$

where $\mathbf{F}^{\mathrm{e}}$ is the elastic deformation gradient incorporating elastic stretch and rotation, while $\mathbf{F}^{\mathrm{p}}$ is the plastic deformation gradient incorporating plastic shearing (Lee, 1969). Here, physically admissible deformation requires $\mathbf{F}^{\mathrm{e}} > 0$ and plastic incompressibility requires $\det \mathbf{F}^{\mathrm{p}} = 1$. The constitutive relations for stress at a material point in the crystal are taken as

$$\mathbf{T}^{\mathrm{e}} = \boldsymbol{C}\left[\mathbf{E}^{\mathrm{e}}\right], \tag{2}$$

where

$$\mathbf{E}^{\mathrm{e}} = \frac{1}{2}\left(\mathbf{F}^{\mathrm{e}^{\mathrm{T}}}\mathbf{F}^{\mathrm{e}} - \mathbf{I}\right) \tag{3}$$

is the total Green–Lagrange strain tensor, $\boldsymbol{C}$ is the fourth-order anisotropic elasticity tensor, $\mathbf{T}^{\mathrm{e}}$ is the 2nd Piola–Kirchhoff stress tensor (a work conjugate to our aforementioned elastic strain measure), and $\mathbf{I}$ is the second-order identity tensor. A flow rule allows for the evolution of $\mathbf{F}^{\mathrm{p}}$ through

$$\dot{\mathbf{F}}^{\mathrm{p}} = \mathbf{L}^{\mathrm{p}}\mathbf{F}^{\mathrm{p}} \tag{4}$$

where $\mathbf{L}^{\mathrm{p}}$ is the plastic velocity gradient, given by

$$\mathbf{L}^{\mathrm{p}} = \sum_{\alpha} \dot{\gamma}^{\alpha} \cdot \left(\mathbf{m}_0^{\alpha} \otimes \mathbf{n}_0^{\alpha}\right), \tag{5}$$

where $\dot{\gamma}^\alpha$ is the plastic shearing rate on the αth slip system, $\mathbf{m}_0^\alpha$ and $\mathbf{n}_0^\alpha$ are time-independent orthonormal unit vectors denoting the slip direction and slip plane normal, respectively, for the αth slip system defined in a fixed isoclinic reference configuration (Kalidindi et al., 1992). The dyadic product in Eq. (5) defines the Schmid tensor, $\mathbf{S}_0^\alpha$. The plastic shearing rate on the αth slip system depends on the resolved shear stress, τ^α, and the slip resistance, s^α, as

$$\dot{\gamma}^\alpha = \widehat{\dot{\gamma}^\alpha}\left(\tau^\alpha, s^\alpha\right), \tag{6}$$

where τ^α is approximated for infinitesimal elastic strains as

$$\tau^\alpha \approx \mathbf{T}^{\mathrm{e}} : \mathbf{S}_0^\alpha, \tag{7}$$

and s^α is usually taken to evolve with $\dot{\gamma}^\alpha$ or other internal state variables, such as the dislocation density (Arsenlis and Parks, 2002; Lee et al., 2010).

2.2. Thermally activated plastic deformation in NC metals

In crystal plasticity, the plastic distortion of the lattice is assumed to arise from the motion of dislocations on well-defined slip systems, which aligns well with the construction of a dislocation-mediated plasticity model for nanocrystals. The influence of the nanoscale grain size on dislocation motion, understood through the nucleation–propagation–absorption process, should then be represented through modifications to the flow law and slip resistances to account for the change in plastic deformation mechanism to a thermally-activated depinning process (Kato, 2009; Wang et al., 2004; Hollang et al., 2006). For thermally-activated plastic flow, it is typical to express the plastic shearing rate, $\dot{\gamma}$, as

$$\dot{\gamma} = \dot{\gamma}_0 \exp\left\{-\frac{\Delta G(\tau_*)}{k_B T}\right\}, \tag{8}$$

where $\dot{\gamma}_0$ is a reference shearing rate, ΔG is the activation free energy for a thermally-activated flow process, τ_* is an effective shear stress, k_B is the Boltzmann constant, and T is the temperature (Kocks et al., 1975). Here, ΔG is a decreasing function of τ_*, defined later, as the work done by τ_* lowers the corresponding activation barrier (Dao et al., 2007). For the thermally-activated depinning process of a dislocation from a GB defect structure, $\Delta G(\tau_*)$ can be approximated by a thermally-sensitive short-range obstacle profile as

$$\Delta G(\tau_*) = G_0\left(1 - \left[\frac{\tau_*}{s_m}\right]^p\right)^q \tag{9}$$

where G_0 is the activation free energy required to overcome the short-range obstacle in the absence of external work, s_m is the effective shear stress required to overcome the short-range obstacle at 0 K, defined later, and both p and q control the shape of the obstacle profile.

The permanent storage of free energy, related to structural changes in the material, cannot be thermally activated as the structure-dictated internal stress is long-ranging in nature (Dao et al., 2007). As a result, the applied shear stress may then be decomposed into thermal and athermal parts accounting for short-range thermal barriers and long-range structural barriers, respectively. The effective (or thermal) shear stress on the αth slip system is

$$\tau_*^\alpha = |\tau^\alpha| - s_{ath}^\alpha \tag{10}$$

where τ^α is the applied shear stress (Eq. (7)) and s_{ath}^α is the athermal slip resistance. As such, it is τ_* that is responsible for overcoming the short-range thermal barriers allowing slip to proceed. The form of Eq. (9) implies that, with increasing T, the short-range thermal barrier to dislocation motion in the slip plane due to the presence of obstacles (GB defect structures) can be overcome at a lower τ^α with assistance from thermal fluctuations (Khan and Liu, 2016). However, if τ^α is lower than s_{ath}^α, thermal fluctuations are not capable of overcoming the short-range energy barrier to initiate slip. The full expression for $\dot{\gamma}^\alpha$ is then constructed with consideration of this as

$$\dot{\gamma}^\alpha = \begin{cases} 0 & |\tau^\alpha| \le s_{ath}^\alpha \\ \dot{\gamma}_0 \exp\left\{-\frac{G_0}{k_B T}\left(1 - \left[\frac{|\tau^\alpha| - s_{ath}^\alpha}{s_m}\right]^p\right)^q\right\} \operatorname{sgn}(\tau^\alpha), & |\tau^\alpha| > s_{ath}^\alpha. \end{cases} \tag{11}$$

The athermal slip resistance can be decomposed to consider contributions from two influences, the grain size, d, and the dislocation density, ρ. As d decreases and the probability for dislocations to pile up at the GBs is reduced, the athermal strength contribution of the grain size, $s_{ath,d}$, is predicted to transition to a d^{-1}-type dependence (Nes et al., 2005). As such, $s_{ath,d}$ is assumed to take the form of an Orowan bow-out stress for a dislocation spanning the nanograin following Kato (2009) and is thus independent of any slip systems. The athermal strength contribution of the dislocation density, $s_{ath,\rho}^\alpha$, is expected to influence both the yield strength and post-yielding behavior of the nanograin with the evolution of ρ and is assumed to take the form of the classical Bailey–Hirsch equation (Bailey and Hirsch, 1960). The full expression for the decomposed s_{ath}^α is then

$$s_{ath}^\alpha = s_{ath,d} + s_{ath,\rho}^\alpha = \frac{\mu b}{2\pi d}\ln\left(\frac{d}{2r_0}\right) + \alpha\mu b\sqrt{\rho^\alpha}, \tag{12}$$

where μ is the anisotropic shear modulus, b is the magnitude of the Burgers vector, r_0 is the inner cut-off radius representative of the dislocation core size, and α is a hardening coefficient.

Note that $s^{\alpha}_{ath,\rho}$ attempts to model the interaction between a propagating dislocation gliding through the nanograin interior with the "forest-like" dislocations contained within the GB plane (or region) that act as pinning obstacles to the mobile dislocation (Malygin, 2007b). Thus the total athermal strengthening in Eq. (12) considers the superposition of the stress required to bow out a dislocation spanning the nanograin interior (pinned at obstacles on the GB) and the internal stress on the dislocation due to interactions with grain boundary "forest-like" dislocations (pinning obstacles in the GB). The "forest-like" grain boundary dislocations of NCs varies from the typical understanding of "forest" dislocations in classical crystal plasticity for large grains. Whereas in large grains, a propagating dislocation will interact (or react) with "forest" dislocations within the grain interior that are immobilized on other slip systems, due to the reduced capacity for dislocation storage in NCs this does not occur (hence the lack of any dislocation interaction matrix in Eq. (12)). Instead in NCs, the propagating dislocation is always in contact with the grain boundaries throughout its lifetime, and therefore, is always interacting with the "forest-like" grain boundary dislocation structure present. These grain boundary dislocations act as the pinning obstacles for the propagating dislocation in the nanograin and provide resistance to the dislocation motion, and this interaction, again, is what the functional form of $s^{\alpha}_{ath,\rho}$ attempts to model here. The athermal strengthening in this case is only assumed to have a square-root dependence on the dislocation density here due to the absence of phenomenological models describing such interactions and is not necessarily the expected behavior of such a phenomenon. Here, μ is defined using the cubic elastic moduli, C_{ij}, as $\sqrt{0.5\left(C_{11}-C_{12}\right)C_{44}}$ (Balasubramanian, 1998). Note that when d is equal to or less than $2r_0$, it is assumed that no grain size athermal strengthening is contributed as the grain size is effectively equivalent to the dislocation core size and the defect can now be considered as a "zone defect" (Chen et al., 2022). Kato et al. (2008) derived an equation for s_m similarly assuming a dislocation bow-out process, but introducing the consideration of a dislocation source length, written as

$$s_m = \frac{\mu b}{2\pi L}\ln\left(\frac{L}{2r_0}\right) \tag{13}$$

where L, the dislocation source length, is the distance between two GB pinning points and should be a fraction of the grain size as $L = cd$ with the parameter c being $0 < c < 1$ (Khan and Liu, 2016). Similar to the grain size strengthening term as noted previously, when d is less than or equal to $d_{crit} = \left(2r_0 \cdot \exp(1)\right)/c$, then s_m remains fixed at the maximal value obtained at d_{crit} to circumvent numerical issues that would arise in the flow law for grain sizes below the critical value due to the assumed form of Eq. (13). This constraint implies that L remains constant as d decreases below d_{crit} requiring c to increase proportionally as a result, potentially violating the previous inequality constraint for very small grain sizes.

After propagation of a dislocation through the nanograin, a plastic shear strain increment on the αth slip system, $\Delta\gamma^{\alpha}$, will be produced on the order of b/d (Khan and Liu, 2016). Since propagation of a dislocation in NCs is assumed to be rate-controlled by the thermally-activated depinning mechanism, the reference shearing rate, $\dot{\gamma}_0$, is formulated as the product of the shear increment and the attempt frequency, ν, of successfully depinning from a pinning obstacle (Hollang et al., 2006). The morphology of the microstructure, particularly grain size and shape, can inform the magnitude of $\Delta\gamma^{\alpha}$ by accounting for the volume of the grain, V_g, and the average αth slip plane area, A^{α}_{swept}, swept by a dislocation during propagation (Bitzek et al., 2008). As such, $\dot{\gamma}_0$ can now be written as a per-slip-system quantity as

$$\dot{\gamma}^{\alpha}_0 = \Delta\gamma^{\alpha}\cdot\nu, \quad \Delta\gamma^{\alpha} = \frac{A^{\alpha}_{swept}\, b}{V_g}, \tag{14}$$

and is substituted into Eq. (11) along with Eqs. (12) and (13). Note that since $\dot{\gamma}^{\alpha}_0$ is a pre-exponential term in Eq. (11), the shearing rate, $\dot{\gamma}^{\alpha}$, is expected to be rather insensitive to small changes in $\dot{\gamma}^{\alpha}_0$ (Kocks et al., 1975). By defining $\dot{\gamma}^{\alpha}_0$ in this manner, $\dot{\gamma}^{\alpha}$ is now scaled by a grain-volume-averaged local shear increment that accounts for the morphology of the grain and any potential variations in the average slip plane area due to the grain shape. Note that Eqs. (11)–(14) together only provide a description of the "propagation" process of plastic deformation in NC metals and do not explicitly account for the "nucleation" process in their formulation due to the assumption that the nucleation of dislocation loops from pre-existing defect sites at the GB will be easier than the depinning process due to the local stress concentrations, as discussed in Section 1.

2.3. Dislocation kinetics considering GB interactions

The critical role of GBs in accommodating dislocation-mediated plasticity of NCs necessitate that the dislocation kinetics be expressed in a form that considers the dislocation-GB interactions. In this way, the dislocation density in the GB is then a balance between the rate of incoming dislocations that have been emitted from pre-existing defect structures and the annihilation (or "absorption") rate of dislocations in the GB (Malygin, 2007b). The storage rate of dislocations accumulating in the nanograin interior is thus dependent on the absorption rate and reducing this significantly, as with deformation at cryogenic temperatures (Wang and Ma, 2004), results in a hardening of the GBs and, subsequently, the nanograin interior (Malygin, 2007a). At room temperatures and above, however, dislocation storage is generally negligible and the increased GB diffusion due to the higher volume fraction of GBs in NCs leads to the generally observed perfect-plastic deformation (Wang et al., 2004; Ovid'ko and Sheinerman, 2003). Here, the GBs are treated as both sources and sinks for dislocations (i.e., nucleation and absorption sites, respectively) and the kinetic equation for ρ as a function of plastic strain, γ, in the GB is expressed by a KME-type model (Mecking and Kocks, 1981; Estrin and Mecking, 1984) as

$$\frac{\partial\rho}{\partial\gamma} = \frac{\partial\rho^{+}}{\partial\gamma} - \frac{\partial\rho^{-}}{\partial\gamma} = \frac{\beta}{bL^{*}} - K\rho, \tag{15}$$

where the generation rate of dislocations emitted from the GB $\left(\partial\rho^{+}/\partial\gamma\right)$, is related to the average mean free path of dislocation motion, L^{*}, and a coefficient determining the intensity of dislocation accumulation, β, while the annihilation rate of dislocations in the GB $(\partial\rho^{-}/\partial\gamma)$ is proportional to the dislocation density scaled by an absorption coefficient, K, that is dependent on temperature, strain rate, and grain size (Malygin, 2007a).

Following Malygin (2007b), the average mean free path is restricted to the grain size (i.e., $L^{*}=d$) due to interactions with the boundary and K is assumed to be related to the rate of absorption of edge dislocations into the GB involving diffusive processes (e.g., diffusive climb of dislocation in the GB). While several processes can account for the rate of absorption of dislocations at the GB, the annihilation of screw dislocation segments by cross-slip is assumed to be inoperative and that the rate of annihilation of edge dislocation segments by dissolution is negligible when compared to the rate of pair annihilation. K can then be written as $K=1/\dot{\gamma}t_{d}$ where t_{d} is the time required for pair annihilation of edge dislocations of opposite sign at the GB, which is expressed as

$$t_{d}=\frac{d^{2}k_{B}T}{4\mu bD_{gb}}, \tag{16}$$

where D_{gb} is the GB diffusion coefficient, defined as $D_{gb}=D_{gb}^{0}\exp\left(-Q_{gb}/k_{B}T\right)$ with D_{gb}^{0} being the pre-exponential factor and Q_{gb} being the activation energy for GB diffusion. The time rate of change of the dislocation density can be written as $d\rho/dt=(d\rho/d\gamma)\,\dot{\gamma}$. Substituting Eqs. (15) and (16) into this expression, the kinetic equation is then expressed in rate form for a particular αth slip system as

$$\dot{\rho}^{\alpha}=\frac{\beta}{bd}\dot{\gamma}^{\alpha}-\frac{4\mu b^{3}}{k_{B}T}\frac{D_{gb}}{d^{2}}\rho^{\alpha}. \tag{17}$$

Note that if the initial dislocation density, ρ_{0}, of the material is non-zero due to processing, the absorption process may still occur during elastic loading, a phenomenon that has been experimentally observed in NC Ni by Adachi et al. via in-situ synchrotron X-ray diffraction (Adachi et al., 2016). As such, it is crucial to consider the influence of a non-zero ρ_{0} on the yielding behavior of nanocrystals as this is regularly neglected in dislocation-density-based crystal plasticity models. This behavior is realized in the present model through the absorption rate in Eq. (17) depending only on the magnitude of dislocation density in the material and not the plastic shearing rate. This results in a difference in evolution of the athermal strength contribution of the dislocation density (see Eq. (12)) before and after macroscopic yielding of the material. The inherent flexibility of the KME-type model formulation facilitates the addition of further dislocation-GB interaction behaviors on the dislocation density evolution, such as a grain size-dependent probabilistic storage rate (Bouaziz et al., 2010) or slip transmission across GBs as a function of misorientation (Hamid et al., 2017).

2.4. Plastic homogenization at the grain-level

As the grain size is reduced into the nanometer range and down towards 1 nm, the classical conception of the dislocation density as a internal state variable (ISV) begins to break down due to the scale similarities between the grain size and the dislocation structures begin considered in NCs. For NCs, the "grain interior"-type dislocation density ISV can no longer represent an abstraction of a complex dislocation substructure, as in classical crystal plasticity for large grains, but would instead be associated directly with discrete dislocations due to the small grain size. Since the primary goal of the present model is to simulate the bulk effect of evolution of the dislocation density at the GBs, directly spatially resolving discrete dislocations in the nanograin interior is not of interest and would present numerous implementation challenges. Instead, by homogenizing the plastic deformation across the grain volume, such spatial resolution issues can be entirely circumvented, simplifying the computational implementation without significant loss of accuracy in simulating the bulk effect of the evolution of the dislocation density at the GBs. It is noted that here, homogenization refers specifically to the enforcement of a grain-uniform plastic deformation and is not conflated with that of more "classical" homogenization schemes common to crystal plasticity modeling, such as the iso-strain assumption of Taylor (1938).

To facilitate the homogenization of the plastic deformation at the grain-level, in line with the concept of the grain-volume-averaged local shear increment of Eq. (14), the dislocation density expressions developed throughout Section 2.3 are similarly made uniform by enforcing a uniform value of $\mathbf{F}^{\mathrm{p}}$ across the grain volume. To maintain this uniformity, the evolution of plastic deformation via the flow rule (see Eq. (4)) must occur in a similarly constrained manner, i.e., the plastic velocity gradient, $\mathbf{L}^{\mathrm{p}}$, must also be grain uniform. As such, the shearing rate, $\dot{\gamma}^{\alpha}$, and thus the accumulated plastic shear strain, $\Delta\gamma^{\alpha}$, should remain constant values for each αth slip system across the nanograin volume over a given time increment. It is clear, however, that the flow law of Eq. (11) admits only a scalar term, τ^{α}, to describe the stress state on an αth slip system to determine the incurred plastic shearing rate. To accommodate this discrepancy, the computational strategy for modeling confined layer slip-based crystal plasticity in nanolaminates developed by Liu et al. (2019) is leveraged. This strategy allows for grain-uniform plastic deformation to be driven by a single grain-volume-averaged elastic stress state while permitting the simultaneous development of heterogeneous elastic deformation throughout the polycrystalline aggregate (or at each integration point) to ensure compatibility of the underlying finite element mesh. The computational details of the present implementation of a grain-volume-averaged elastic stress state driving grain-uniform plastic deformation and the resulting modifications to the solution procedure are given in Appendix A. The impact of this assumption of grain-level homogenized plastic deformation on the development of slip activity is discussed at length in Appendix C.

This homogenization assumption discussed here is also reasonably necessitated by the significant disparity between the typical dislocation core size range ($2r_{0}$ or 2 nm–3 nm) and the nanometer grain size range (1 nm–100 nm) being considered. The discrete

nature of dislocation activity within the grain interiors at the nanometer length scale leads to a situation in which continuum-based models begin to break down. The present plastic homogenization strategy, however, allows for an approximation of the plastic deformation of the grains induced by discrete dislocation motion to be accounted for by "coarse-grained" shearing behavior. As a result, the model can readily simulate the overall evolution of plastic deformation within a nanograin while also providing a reasonable description of the bulk nanocrystalline aggregate deformation response. It is also noted that the omission of grain-boundary-mediated plastic deformation mechanisms in the present model formulation enables the exploration of the functional limits of dislocation-mediated plasticity in NC deformation as the grain size is varied, as such, the model may be expected to break down under certain conditions when compared to available experimental data due to this intentionally limiting assumption.

3. Model implementation

The crystal plasticity model proposed in Section 2 is implemented with multi-threading through the user subroutines UMAT and UEXTERNALDB in ABAQUS (Smith, 2009) following the implicit time-integration scheme of Kalidindi et al. (1992). The analytical material Jacobian matrix derived by Balasubramanian (1998) is incorporated into the solution scheme to improve the rate of convergence along with the modifications of Alankar et al. (2009) which facilitate the evolution of the dislocation density as an internal state variable. The overall solution scheme is as follows: At the start of a new increment at time t, an estimate of the total deformation gradient, $\mathbf{F}(\tau)$, at the end of the time increment, time $\tau = t + \Delta t$, is provided, along with $\mathbf{F}(t)$, $\mathbf{F}^{\mathrm{p}}(t)$, and $\rho^{\alpha}(t)$, known from the previous increment. From this, the local Cauchy stress, $\boldsymbol{\sigma}(\tau)$, obtained via the two-level iterative scheme of Kalidindi et al. (1992), and the analytical material Jacobian matrix, defined later, must then be computed along with the evolution of the plastic state variables, $\mathbf{F}^{\mathrm{p}}(\tau)$ and $\rho^{\alpha}(\tau)$. In an implicit finite element scheme, the estimated displacements are iteratively revised until the stress field satisfies the principle of virtual work at the end of the increment (Kalidindi et al., 1992; Simo and Hughes, 1998). Here, the material Jacobian matrix is used in a Newton-type iterative scheme to revise the estimated displacements, however, it only affects the rate of convergence and not the solution accuracy (Nguyen and Waas, 2016).

In the implementation, the subroutine UEXTERNALDB is utilized for the initialization of the simulation, processing input data files, and updating the solution state at both the beginning and end of an increment. The subroutine UMAT performs the computations necessary to solve the constitutive model, however, due to the grain-level plastic homogenization assumptions discussed in Sections Section 2.4, the computations may be performed at the grain-level and integration-point-level separately, as discussed in the appendices. A MODULE is used to provide all subroutines access to the initialized storage arrays for either retrieval or updating as necessary. To maintain thread safety during data writes to shared arrays in the MODULE, a MUTEXLOCK is used around critical sections in the UMAT, allowing only a single thread to write data to shared arrays at a time, which are initialized using MUTEXINIT in UEXTERNALDB. Two flag variables are utilized during the solution scheme, one to record if the grain-level computation for a particular grain has been previously completed at different integration point (IP) and another to record if all IP-level computations have been completed for the current iteration. The latter is only used to reset the grain-level computation flag after completion of an increment, successful or not, to ensure the grain-level computations are performed each time UMAT is called by ABAQUS. The grain-level computation is only performed by the first IP encountered by ABAQUS for a particular grain across all threads. As ABAQUS loops through all IPs sequentially, even when multi-threaded, the use of flag variables and mutexes ensure that subsequent IPs do not attempt to perform the grain-level computation once a solution has been obtained. A flowchart of the implemented solution procedure is presented in Fig. 1 for the ith IP contained within the gth grain. The implemented grain-level and IP-level computational procedures are presented in more detail in Appendices A and B, respectively.

4. Results and discussion

4.1. Simulation instantiation

Equiaxed polycrystalline aggregates of varying grain size distributions with uniform distributions of crystallographic orientations (also referred to as "random" or "uniform" texture) are tessellated and meshed with second-order tetrahedral elements using *Neper* (Quey et al., 2011) as cubic domains with edge length unity, shown later in Figs. 4(b) and 4(c). The generated files describing the polycrystalline aggregate (tessellation, crystallographic orientations, element statistics) are imported into MATLAB to process microstructural information necessary to initialize the simulation. For each grain in the polycrystalline aggregate, the volume relative to the mesh is computed from the convex hull of its vertices and the grain size is estimated as the spherical equivalent diameter. The physical grain size distribution of the aggregate is then obtained by scaling the mean of the grain size distribution relative to the mesh to the prescribed physical value. From this, the physical grain volume for each individual grain is retrieved by scaling the vertices so that the re-computed convex hull volume produces the expected physical grain size.

The initial grain volume and surface area are recorded and written to their respective input files. Euler–Bunge angles generated by *Neper* for the grain are used to rotate the crystal lattice into the sample frame after which the intersection area between the grain surface and a slip plane is computed using the matGeom library (Legland, 2023). This intersection computation is repeated at 25 uniformly spaced points spanning the grain and then averaged for each αth slip system to determine A^{α}_{swept}. The resulting values are written to an input file, noting that there will only be variation in the value of A^{α}_{swept} between the slip planes. The ρ_0 prescribed for the simulation is constant for all grains in the aggregate and is uniformly distributed among the slip systems for a given grain (Arsenlis and Parks, 2002), then written to an input file. Additional input files that are generated include: an ABAQUS input file containing mesh information and simulation boundary conditions, a list of per-element crystallographic orientations, initial element

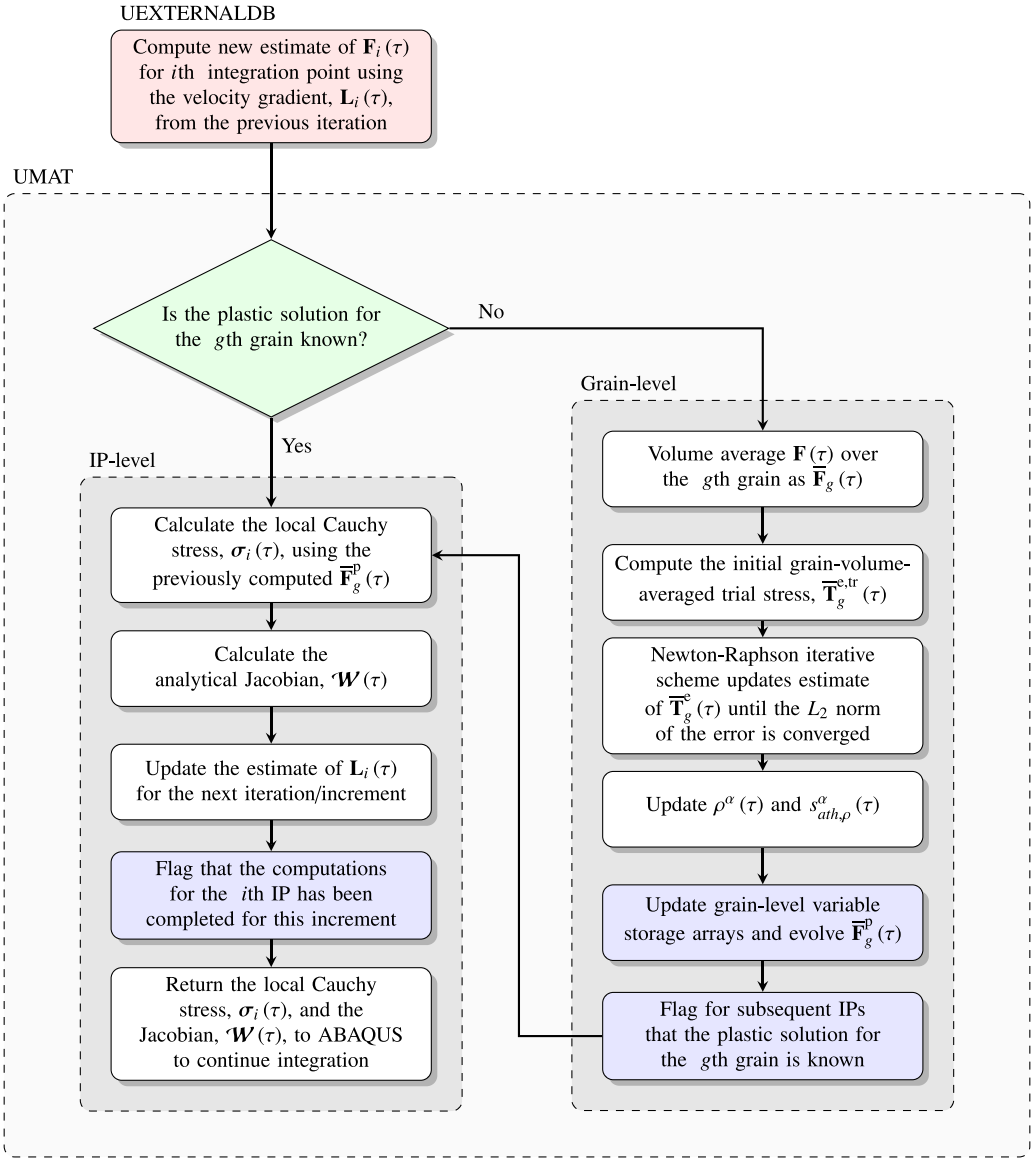

Fig. 1. A flowchart showing the implemented solution procedure for a single ith integration point (IP) contained within the gth grain in the polycrystalline aggregate. Note that steps performed within the subroutine UEXTERNALDB are colored red, steps performed within a MUTEXLOCK are colored blue, and decisions are colored green. (For interpretation of the references to color in this figure legend, the reader is referred to the web version of this article.)

volumes, an element-to-grain index, and definitions of the slip systems α. Lastly, a configuration file containing model parameters and information about the mesh/microstructure required to properly dimension storage arrays is introduced into the MODULE using an INCLUDE statement for flexibility of instantiation.

Simulations performed throughout this section, unless otherwise noted, are designed to reproduce the experimental conditions of the room temperature ($T = 296$ K) compression at a constant engineering strain rate, $\dot{\epsilon}$, of 10^{-4} s^{-1} on bulk samples of NC Cu of Khan et al. (2008). Simple uniaxial compression is performed on the simulated aggregates along the direction of the z axis. The bottom $x-y$ face has normal motion constrained while the top $x-y$ face has a velocity applied to the nodes matching the aforementioned strain rate. The remaining faces are traction-free. A single node $(x, y, z = 0)$ is fully constrained and two nodes $(x = 0, y = 1, z = 0$ and $x = 1, y = 0, z = 0)$ are constrained in the x and y directions, respectively, to prevent rigid body motion.

4.2. Parameter calibration

The crystal plasticity model was calibrated simultaneously to experimental true stress–strain curves of NC Cu for three average grain sizes, $\bar{d}$, (32 nm, 51 nm, and 118 nm) at a strain rate of 10^{-4} s^{-1} and two increased strain rates (1 and 10^{-2} s^{-1}) for a grain

Table 1
The calibrated model parameters for the NC Cu produced by ball-milling of Khan et al. (2008).

G_0 [eV]	p	q	D^0_{gb} [nm^2/s]	Q_{gb} [eV]	α	ρ_0 [nm^{-2}]	c	ν [Hz]	r_0 [nm]	β
1.025	0.99	1.01	3.903×10^{11}	0.862	0.2995	9.3×10^{-4}	0.2784	1.7×10^{10}	1.243	0.01

Table 2
The lower and upper bounds used during the calibration of the model parameters.

Bound	G_0 [eV]	p	q	D^0_{gb} [nm^2/s]	Q_{gb} [eV]	α	ρ_0 [nm^{-2}]	c	ν [Hz]	r_0 [nm]	β
Lower	0.85	0.50	1.00	1×10^{11}	0.70	0.01	1×10^{-5}	0.25	1×10^{10}	0.511	0.01
Upper	2.00	1.00	1.50	1×10^{13}	1.00	0.30	1×10^{-3}	1.00	1×10^{11}	2.045	1.00

size of 32 nm, to ensure the calibrated model captured both the grain size strengthening and rate-dependence of the experimental NC Cu. Simultaneous curve fitting was carried out to 10% true strain, ϵ, using a constrained optimization algorithm (FMINCON) in MATLAB. During calibration, the microstructure and associated finite element mesh (defined later) remain constant, with only the physical grain size being scaled as needed. A MATLAB script can then import the associated polycrystal files and generate several job source file directories with input files written specifically for each job, carrying information such as the strain rate, grain volumes, etc, as mentioned previously in Section 4.1. During calibration, however, only the configuration input file and the initial dislocation densities need to be modified upon each perturbation of the optimizer. The parameter bounds (see Table 2) and the initial parameter guesses are "min–max" normalized to fall with the interval [0:1], such that the interior-point algorithm can properly sample the parameter space as some parameters can vary by several orders of magnitude. The constrained optimization function, FMINCON, is employed using nested anonymous functions to facilitate the passing of variables defining the simulation setup to successive perturbations of the optimizer in a convenient way. ABAQUS jobs are executed by MATLAB, and upon completion, output data files are imported back into MATLAB to compute the volume-averaged stress–strain curves for all calibration cases. The difference in stress between the experimental and simulated stress–strain curves are computed along the calibrated strain range at fixed intervals for each case, creating multiple separate vectors of stress error values. These separate stress error vectors are then concatenated and the Euclidean norm of the concatenated vector is computed, providing the global error quantity for the optimizer to minimize.

The final set of calibrated model parameters for NC Cu are provided in Table 1. It is noted that as the model parameters here are calibrated only to macroscopic stress–strain data, they should not be considered unique. Despite this, the simultaneous calibration to multiple stress–strain curves is expected to mitigate the possibility for a poor fitting of the model parameters. Since the goal of the present model is to simulate the bulk deformation of NCs, any potential differences in local deformation response that would arise from a non-unique set of calibrated model parameters should not significantly impact the simulated results presented throughout the present work (Hochhalter et al., 2020). The material-specific C_{ij} and b for Cu are held fixed during optimization at $C_{11} = 168.4$ GPa, $C_{12} = 121.4$ GPa, $C_{44} = 75.4$ GPa, and $b = 0.2556$ nm (Lide, 2009). The remaining model parameters are constrained by the bounds provided in Table 2. These bounds were informed from reported values in the literature, either from experiment or simulated works, by limits required by previously defined inequalities, such as for c, or by typical values in the literature, such as for α or r_0. For certain parameters, i.e., G_0, p, q, and c, manual adjustment of one or both of the bounds to ensure a stable calibration process.

The bounds for G_0 were informed by the modeling work of Kato (2009) and Khan and Liu (2016), the experimental work of Khan et al. (2008), used in calibration, informed the value ρ_0 which was set to span several orders of magnitude near the lower end of the experimentally reported dislocation densities in NCs due to the preparation method of the samples. Both D^0_{gb} and Q_{gb} were informed by the experimentally reported values of grain boundary self-diffusion in high purity Cu from Surholt and Herzig (1997). The parameters p, q, and c, are functionally defined by inequalities with $0 < p \leq 1$, $1 \leq q \leq 2$, and $0 < c < 1$, where both p and q inequalities are referenced from Kocks et al. (1975) and the inequality for c is provided by Kato et al. (2008). Note that all three inequality terms had one of their bounds manually adjusted prevent numerical issues during the automated calibration process. The lower bound for the hardening coefficient, α, is informed from the numerical work of Khan and Liu (2016). The attempt frequency, ν, is allowed to span an order of magnitude, however, the value is lower than typically expressed (i.e., the Debye frequency or $\sim 10^{13}$ Hz) to facilitate the time-scale transition of the dislocation processes as described by Sobie et al. (2017). Lastly, the bounds for β are informed by the numerical modeling work of Zhao et al. (2019) and that of Malygin (2007b), while the bounds for the inner cut-off radius, r_0, are set to the typical range of $2b$ to $10b$.

A polycrystal consisting of 64 cubic, equi-volume grains (1536 elements) with a uniform distribution of crystallographic orientations was selected for calibration as it was found to provide a good balance between computational cost and accuracy in deformation response for optimization, while mitigating the influence of a particular grain size distribution shape and texture on the resulting model parameters. Note that doubling the number of grains in the same microstructure (128 equi-volume, cubic grains, 12,288 elements) was found to change the magnitude of the stress measured at 5% true strain by only 3 MPa or 0.42% difference relative to the 64-grain polycrystal. Similarly, utilizing the full ~500 grain polycrystals (~60k elements) described later in Section 4.3 was found to change the magnitude of stress measured at 5% strain by approximately 7 MPa or a 1% difference. This minor variation in accuracy was accompanied by order of magnitude increases in wall-clock times to simulate the strain range necessary for calibration which, when compounded with the number of simulations required for optimization (~1k due to Jacobian approximations for FMINCON and simultaneous fitting to 5 stress–strain curves), was deemed an acceptable loss in accuracy to drastically reduce computational cost.

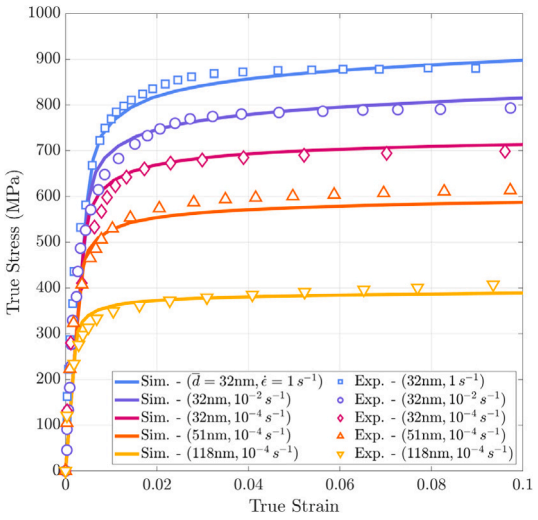

Fig. 2. The simulated true stress–strain responses (lines) after calibration deformed at different grain sizes and strain rates along with the corresponding experimental data (symbols) of Khan et al. (2008) which was used for the calibration process. (For interpretation of the references to color in this figure legend, the reader is referred to the web version of this article.)

The sensitivity of the simulated deformation response to variations in the individual calibrated model parameters is investigated by perturbing the model parameters by ±10% of their value and comparing the differences in the 0.2% offset yield stress as compared to the calibrated baseline. Note that since their calibrated values are close to their upper bounds, both p and α are instead perturbed by −10% and −20%. Similarly, the parameters q and β are close to their lower bounds and are instead perturbed by +10% and +20%. Sensitivity simulations were performed using the full 474 grain normal distribution polycrystalline aggregate, described later in Section 4.3, deformed in uniaxial compression to a true strain of 10% at a strain rate of 10^{-4} s^{-1}. It is found that the model is relatively insensitive to small changes in D^0_{gb}, c, ν, ρ_0, α, and β with the largest perturbations resulting in no more than a 2.59% difference in the yield stress across the parameters, with an average difference of 0.79%. The model is most sensitive to changes in G_0, p, q, r_0, and Q_{gb} as these parameters control the flow law and the slip resistances for the model. Particularly, the value of G_0 impacts the magnitude of the stress–strain curve with the 10% perturbations resulting in an average difference of 6.78% in yield stress, while for the largest perturbation, the remaining parameters together produced an average difference of 4.06% in the yield stress. It is emphasized here that the calibrated model parameters presented in Table 1, particularly for parameters related to more discrete dislocation-based phenomena, such as ν or c, can be effectively considered as "averages" for the simulated bulk NC Cu samples presented here. While some statistical and/or spatial variation may be possible for these parameters, due to the relative insensitivity of the macroscopic model performance to small perturbations of these parameters, it is not likely that any reasonable statistical/spatial variations in the parameters would notably impact the simulated trends presented throughout the rest of the manuscript. Such statistical/spatial variations also would need to be sampled from an assumed statistical distribution for each model parameter, introducing further uncertainty into the model predictions, as no experimental data is available to reasonably justify any specific choice of distribution.

Fig. 2 shows good agreement of the simulated stress–strain responses to the experimental data with the final set of calibrated model parameters. Note that the model is not directly calibrated to temperature-dependent data, such as that of Farrokh and Khan (2009). It was expected that, since the shearing rate (Eq. (11)) is based on a thermally-activated mechanism, calibrating the model to strain-rate-dependent experimental data should also reasonably capture the temperature-dependence. This decision was also motivated by the possibility for transient grain growth during the deformation of the experimental NC Cu samples at elevated temperatures as such microstructural instabilities would influence the overall model calibration process due to the present model not accounting for such processes. However, the influence of grain growth due to the ambient temperature is expected to be minimal over the time scales simulated in the present work (Gertsman and Birringer, 1994). Note that we do not dismiss the potential for stress-driven grain growth occurring in physical NC materials, even at room temperature, as this has been experimentally observed previously in mechanical testing of NC Cu samples (Zhang et al., 2004; Frazer et al., 2020), however, it must considered inoperative here due to the paucity of experimental data with which to calibrate a stress-driven grain growth model in conjunction with the previously outlined macroscopic calibration process to experimental stress–strain data. This is an inherent limitation of the present model formulation and the results presented throughout the remainder of the section are presented with the caveat that the microstructure is "static" during deformation, i.e., no grain growth occurs. After the model calibration process was complete, the capability for the model to capture the temperature-dependence of the deformation was compared to experimental data from Farrokh and Khan (2009). Fig. 3 compares the model predictions with the final set of calibrated parameters to the experimental data of Farrokh and Khan (2009) where a 32 nm average grain size NC Cu sample is deformed at $\dot{\epsilon} = 10^{-2}$ s^{-1}, at various temperature (T = 233 K, 296 K, 375 K, and 425 K). Good agreement with the experimental data is found out to 10% true inelastic strain, with only notable deviations occurring in the case of T = 375 K, where the simulated results under predict the magnitude of the stress, and

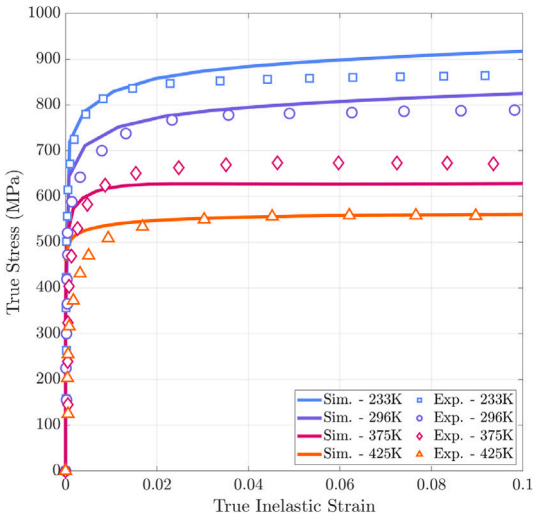

Fig. 3. The simulated true stress vs. true inelastic strain deformation responses (lines) as a function of temperature along with the corresponding experimental data (symbols) of Farrokh and Khan (2009) which was omitted during the calibration process. (For interpretation of the references to color in this figure legend, the reader is referred to the web version of this article.)

in the case of $T = 425$ K where the softer behavior near the knee of the stress–strain curve is not captured by the simulation. The reasonable performance of the model in capturing the temperature-dependence despite such data being omitted during the initial calibration process gives confidence in the model predictions made at room temperature ($T = 296$ K) throughout the remainder of the present work.

4.3. Yield strength

It is well known that the yield strength of crystalline metals is sensitive to the grain size. When the grain size is reduced into the UFG and NC regimes, however, the strength is also impacted by the processing state of the material (Khan et al., 2008). As such, the combined effect of the average grain size and its associated distribution shape, described by the mean, μ, and standard deviation, σ, along with the initial dislocation density on the 0.2% offset yield strength can be systematically explored with the present model. Average grain size values are chosen spanning the range of the nanoscale regime (5, 7, 10, 14, 22, 32, 51, and 118 nm) facilitating the exploration of Hall–Petch strengthening or any deviation from coarse-grained extrapolation of Hall–Petch trends (Meyers et al., 2006). A narrow, normal distribution shape ($\mu = 1$, $\sigma = 0.05$) is assumed to represent the experimental grain size distribution in the NC Cu prepared in Khan et al. (2008) by ball milling and consolidation, and a wide, log-normal distribution ($\mu = 1$, $\sigma = 0.275$) following the experimental distributions reported by Dalla Torre et al. (2005) in ED NC Ni, are selected to explore the effect of distribution shape on mechanical strength.

Fig. 4(a) shows the ideal, normalized grain size distributions utilized in this study compared to the respective actual distributions from the generated polycrystalline aggregates. The normal distribution polycrystal mesh utilized for the simulations contains 474 grains (57,166 elements, 120 elements per grain, Fig. 4(b)) while the log-normal distribution polycrystal mesh contains 475 grains (55,867 elements, 117 elements per grain, Fig. 4(c)), both with initially uniform distributions of crystallographic orientations. It was found that increasing the number of elements in the mesh to approximately 230 elements per grain resulted in only a 0.1% change to the measured macroscopic stress and 0.02% change to the dislocation density values at 5% strain. Note that the number of elements in the mesh was varied by changing the relative characteristic length or 'rcl' in *Neper*, which facilitates mesh refinement without impacting the morphology of the grains. As the average grain size value is varied for a particular grain size distribution, the meshed polycrystalline aggregate and the input crystallographic orientations are held fixed. Only physically scalable input quantities, such as the grain volumes or initial dislocation densities, are adjusted along with the average grain size. The initial dislocation density is set to the calibrated value of 9.3×10^{-4} nm^{-2} (or 9.3×10^{14} m^{-2}) and an increased value of 10^{-2} nm^{-2} (10^{17} m^{-2}) which is representative of the observed dislocation densities measured experimentally in materials prepared by SPD.

Fig. 5 shows the simulated results of the 0.2% offset yield strength as a function of average grain size compared with the experimental results of Meyers et al. (2006) for the yield strengths of NC Cu prepared by a variety of methods, as well as the experimental data of Khan et al. (2008) used in model calibration. Good agreement is found between the yield strengths of the simulated and the experimental bulk NC Cu with the model able to accurately capture the magnitude of the experimental yield strength for the 22 nm grain size polycrystal which was not included in the calibration data set. The normal distribution exhibits a higher strength that the log-normal distribution across the nanoscale regime, however, the yield strengths become comparable as the grain size is reduced towards 5 nm. This is an expected result as the wide tail of the log-normal distribution allows for the presence of significantly larger grains in the polycrystal, which have a lower strength per Eqs. (12) and (13), leading to a larger volume

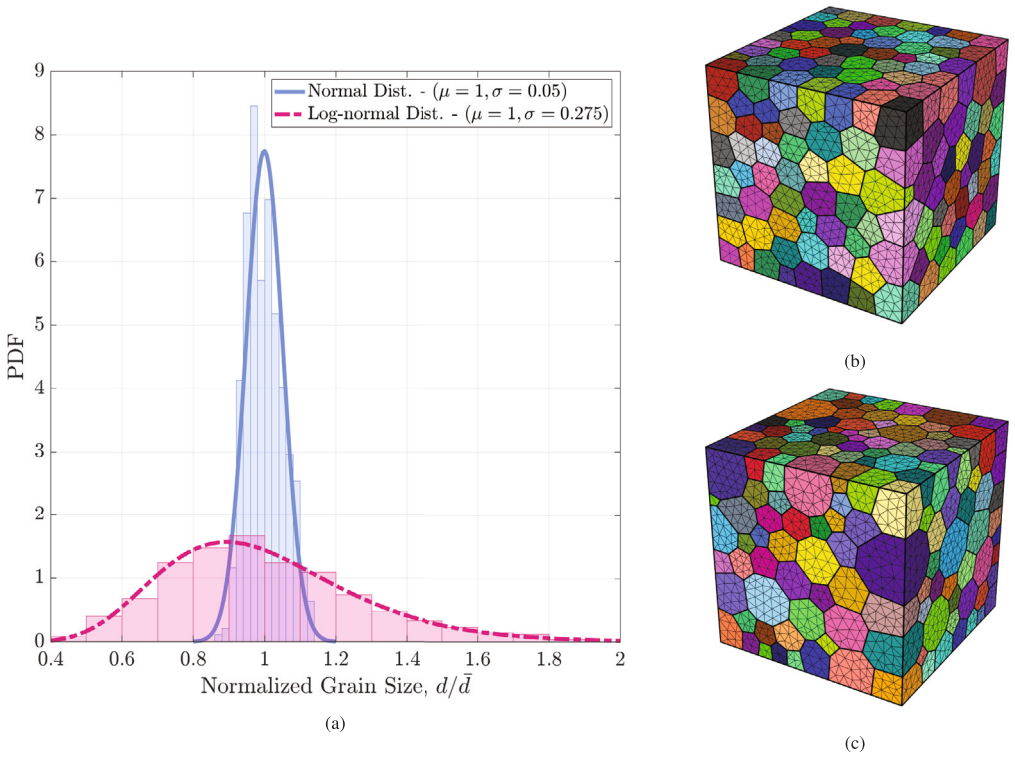

Fig. 4. (a) Normal and log-normal grain size distributions normalized by the average grain size, $\bar{d}$, (such that the mean values, μ, are 1) representing the experimental grain sizes distributions reported by Khan et al. (2008) and Dalla Torre et al. (2005), respectively. Here, the standard deviations, σ, of 0.05 and 0.275 produce a narrow normal distribution and a wide log-normal distribution, respectively. (b) Meshed polycrystalline aggregate with the normal grain size distribution of (a) with 474 grains. (b) Meshed polycrystalline aggregate with the log-normal grain size distribution of (a) with 475 grains. Note that in (b) and (c) each grain is colored arbitrarily. (For interpretation of the references to color in this figure legend, the reader is referred to the web version of this article.)

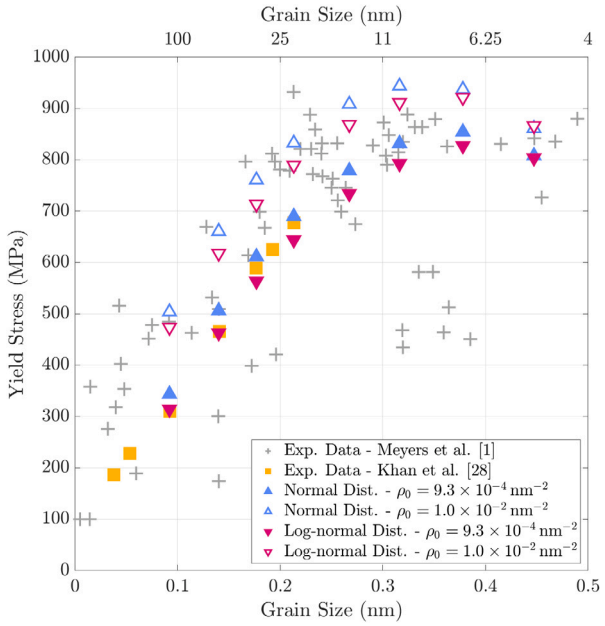

Fig. 5. Simulated results of the 0.2% offset yield strength of NC Cu as a function of grain size, distribution shape, and initial dislocation density, ρ_0, compared to experimental data from Meyers et al. (2006) (cross markers) and the experimental data from Khan et al. (2008) (square markers), the latter of which was used for model calibration.

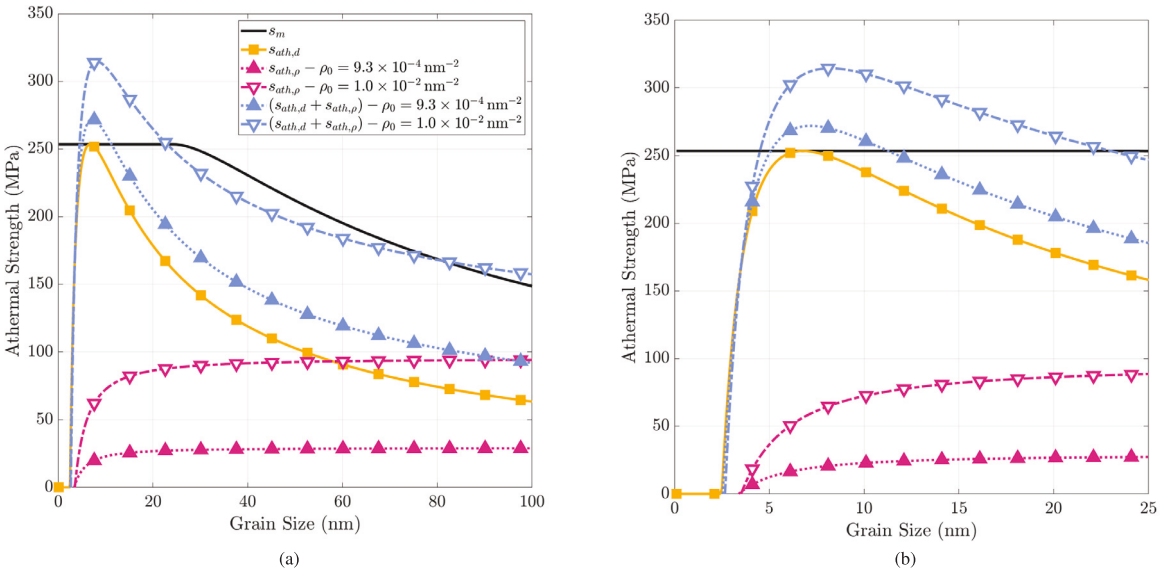

Fig. 6. Variation in athermal strength contributions as a function of grain size and initial dislocation density sampled at the 0.2% offset yield stress for the normal grain size distribution polycrystals across (a) the nanometer range and (b) the subset of the nanometer range where s_m is made a constant value. The grain sizes where $s_{ath,total}$ are found to be 7.2 nm and 8.2 nm for the calibrated and increased values of initial dislocation density, ρ_0, respectively.

fraction of the polycrystal plastically saturating earlier during deformation resulting in a lower yield strength. Further, it is found that increasing the initial dislocation density bounds the majority of the scatter in the experimental data well, despite neglecting the presence of GB-mediated plasticity. These simulated results highlight the interplay between the average grain size, the shape of the grain size distribution, and the initial dislocation density on the bulk strength of the synthesized NC.

A notable deviation from the coarse-grained Hall–Petch extrapolation is observed for average grain sizes below 30 nm in the simulated results with an inverse Hall–Petch behavior observed for all cases as the grain size is reduced below approximately 7 nm. As the d_{crit} that maximizes s_m for the utilized model parameters is 24.3 nm, the presence of an inverse Hall–Petch effect at lower grain sizes should be a result of the athermal strengthening terms in the proposed model. Fig. 6(a) shows how the athermal strength terms in the model vary as a function of grain size and initial dislocation density sampled at macroscopic yielding (i.e., 0.2% offset yield point) across the nanometer range. While s_m and $s_{ath,d}$ are analytical and can be plotted directly, values of $s_{ath,\rho}$ are first extracted from simulated results, averaged over the slip systems and polycrystal volume, and then fit with a two-term power function using MATLAB (R^2 in both cases greater than 0.99). This provided a smooth approximation of $s_{ath,\rho}$ across the nanometer range allowing $s_{ath,total} = \left(s_{ath,d} + s_{ath,p}\right)$ to be easily computed.

The grain size athermal strength contribution ($s_{ath,d}$) peaks at 6.75 nm for the present simulations, resulting in the 7 nm grain size polycrystal having a higher average $s_{ath,d}$ (~250 MPa) than either the 5 nm or 10 nm grain size polycrystals (~240 MPa in both cases) despite the presence of a grain size distribution. The athermal strengthening contributed from the dislocation density $\left(s_{ath,\rho}\right)$, however, evolves with strain, with the dislocation density magnitude decreasing in the elastic regime here due to the lack of dislocation nucleation at low stresses. As the rate of annihilation is inversely proportional to the square of the grain size, the smallest grain sizes reach the lowest dislocation density magnitude prior to macroscopic yielding. This can be seen directly in Fig. 6(b) as the value of $s_{ath,\rho}$ approaches zero for both cases of initial dislocation density around a grain size of ~3.5 nm. At the 0.2% offset yield point, considering the case where $\rho = 9.3 \times 10^{-4}$ nm^{-2}, the dislocation density at a grain size of 5 nm only contributes a strengthening of 12.36 MPa, reduced from 18.69 MPa and 22.8 MPa from the 7 nm and 10 nm grain sizes, respectively. A similar decrease from 72.34 MPa to 36.52 MPa is seen for the case where $\rho = 1.0 \times 10^{-2}$ nm^{-2}, when the grain size is decreased from 10 nm to 5 nm. For both cases of ρ_0, however, $s_{ath,d}$ and s_m remain consistent. By computing the total athermal strength contribution, $s_{ath,total}$, it can be seen that the variation in $s_{ath,\rho}$ result in a shift of the peak strengthening to the right from the peak value of $s_{ath,d}$ at a grain size of 6.75 nm with the maximal values of $s_{ath,total}$ being found at ~7.2 nm and ~8.2 nm for the calibrated and increased values of ρ_0, respectively. This agrees with the results of Fig. 5 where the inflection point is observed around a grain size of 7 nm. Thus, the inverse Hall–Petch effect observed in the simulated results are the result of the rapid drop-off in grain size strengthening from $s_{ath,d}$ as grain size is reduced below 6.75 nm combined with the simultaneous drop-off in dislocation density strengthening from $s_{ath,\rho}$ as grain sizes approach zero, although it seems that the form of $s_{ath,d}$ primarily drives the observed behavior due to the magnitude of strength contributed relative to $s_{ath,\rho}$.

4.4. Strain rate-sensitivity

The strain rate-sensitivities of NCs have been commonly reported to be at least an order of magnitude higher than that of their coarse grained counterparts (Lu, 2016). The dominant plastic deformation mechanism in coarse grained materials is forest cutting

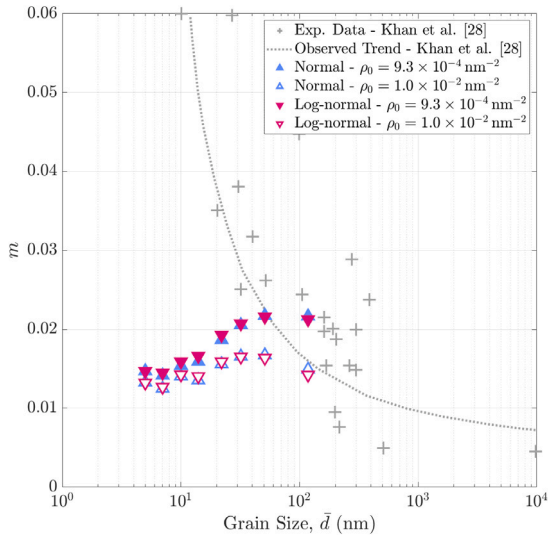

Fig. 7. Simulated results of the strain rate-sensitivity of NC Cu as a function of grain size, distribution shape, and initial dislocation density, compared to the experimental data and observed trend guideline referenced from Khan et al. (2008).

dislocations (Frost and Ashby, 1982), resulting in a low rate-dependence and a high activation volume. However, as the grain size is reduced into the nanometer regime, the relatively increased volume fraction of GBs in the material leads to the plastic deformation mechanism being dominated by dislocation-GB interactions increasing the rate-dependence and severely decreasing the activation volume (Chen et al., 2006). The strain-rate sensitivity, m, is defined at a constant strain and temperature as

$$m = \left. \frac{\partial \ln \sigma_f}{\partial \ln \dot{\epsilon}} \right|_{\epsilon,T}. \tag{18}$$

where σ_f is the flow stress. Here, following the experimental procedure of Khan et al. (2008), m is calculated by recording the flow stress reached at 2.5% strain after deforming the simulated aggregates at $\dot{\epsilon}$ varying from 10^{1}–10^{-3} s^{-1}.

Fig. 7 shows the variation of m with the grain size (5, 7, 10, 14, 22, 32, 51, and 118 nm) and distribution shape as simulated at the two initial dislocation densities utilized in Section 4.3 and compared to experimental data of NC Cu prepared by a variety of methods as referenced from Khan et al. (2008). It is found that when grain sizes are larger (i.e., greater than 75 nm), the simulated results show a wide variation in m, as a result of varying the initial dislocation density. Despite this, the magnitudes of the simulated values of m at these increased grain sizes agrees well with the experimental data. This agrees with the expectations that dislocations are still the dominant carries of plasticity at these increased grain sizes. The variation in m at these increased grain sizes is comparable to the scatter observed in the experimental data of Khan et al. (2008). This suggests that the scatter observed in the experimental data may result from variation in the initial microstructural state (i.e., initial dislocation density) as a result of different processing routes for the NCs.

This is important to note as the strain rate-sensitivity of a material is influenced by both intrinsic and extrinsic factors, meaning that both the overall microstructure and the loading conditions during the experiment influence the measured result, respectively. As in both the experiment and the simulation the loading conditions are controlled, any variation observed in measured values of m would most reasonably arise from variations in the microstructure of the material. This can be evidenced from the experimental data in Fig. 7 where, for a similar grain size, the reported values of m are seen to vary notably. It can be reasoned that other microstructural factors, separate from the grain size, such as the grain size distributions or the structure of the GBs which can be significantly influenced by the processing route of the material, then should produce such variation. Thus, the choice of processing route and the resulting strain rate-sensitivity of the material are inextricably connected, a conclusion supported by the simulated results in Fig. 6, where varying the initial dislocation density at the GBs (representative of varying the processing route of the material) produces a similarly wide variation in measured values of m, comparable to the spread observed in the experimental data. The shapes of the grain size distributions explored here have a minimal effect on the magnitude of m with maximum difference between the two distributions of 6.84×10^{-4}, being an order of magnitude less than the experimental variation in m reported by Chen et al. (2006).

As the grain size is reduced, however, a decreasing trend in m is observed for all cases which deviates considerably from the experimental trend. It is emphasized that the inability of the simulated results presented here to capture the observed experimental trend in m is an expected result of the model formulation. As only dislocation-mediated plasticity is considered in the construction of the model, this is the only plastic deformation mechanism that can contribute to the rate-sensitivity observed from the model. The significant increase in m observed in NCs as the grain size decreases is generally attributed to the dominance of GB-mediated plastic deformation mechanisms which boast a significantly large m (e.g., 0.5 for GB sliding (Gifkins, 1976)). Therefore, as the present

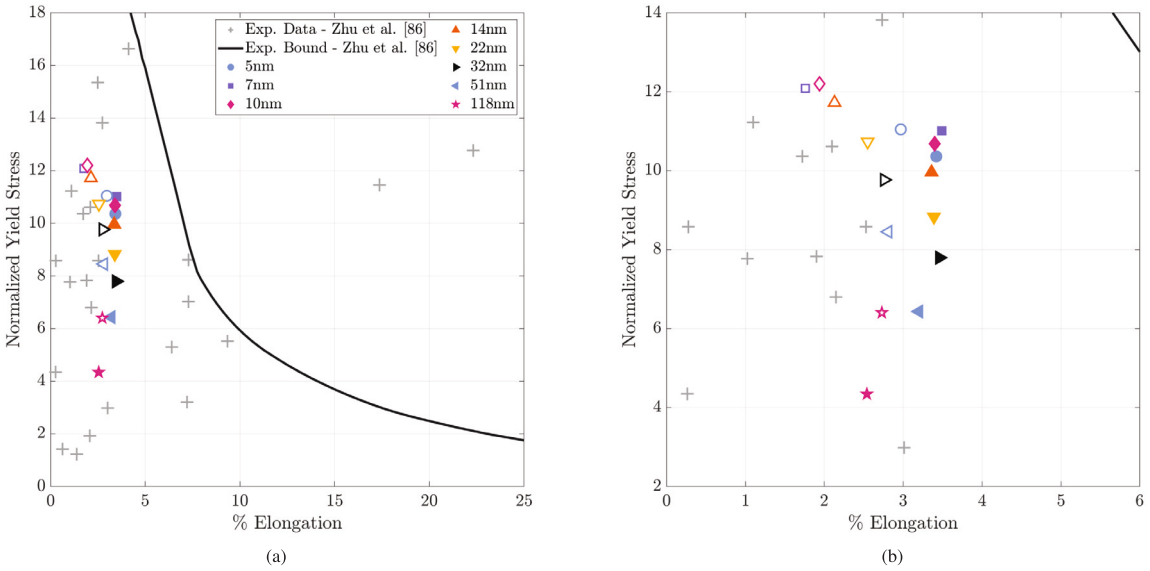

Fig. 8. (a) Experimental yield stresses of various NC materials normalized by their coarse-grained counterpart yield stress as a function of % elongation referenced from Zhu and Liao (2004) compared to simulated results for NC Cu. Simulated results for NC Cu polycrystalline aggregate with a normal grain size distribution are shown as a function of grain size and initial dislocation density. (b) Zoomed in version of (a) highlighting the influence of the grain size and initial dislocation density on the change in strength and % elongation. Note that simulated results for the calibrated value of initial dislocation density have closed (or filled) markers while simulated results with an increased value of initial dislocation density have open markers. Note that the majority of the observed experimental data lies on the left side of the observed bound line denoting the typical regime of high strength, but low ductility.

model neglects these GB-mediated plastic deformation mechanisms, the rate-sensitivity predicted by the model instead decreases with grain size as observed. It is noted, however, that this phenomenon has been previously reported experimentally in some FCC materials (Husain et al., 2020; Jeong and Kim, 2023). Increasing ρ_0, interestingly, results a decrease in the magnitude of m with this effect diminishing as the grain size is reduced. The activation volume, $V^* = \sqrt{3}k_B T\,(\partial \ln \dot{\epsilon}/\partial \sigma)$, for all simulated cases increased from approximately 25 b^3 to 50 b^3 across the nanometer range explored here. The observed range shows reasonable agreement with experimental literature for NC Cu of 8 b^3 to 40 b^3 as reported in Chen et al. (2006) for a similar range of grain sizes.

4.5. Influence of initial dislocation density on the ductility

While NC metals typically show a significant increase in their strength when compared to their coarse-grained counterparts, this gain in strength is usually accompanied by a significant decrease in ductility, limiting the viability of using NC metals in any structural application (Challapalli Suryanarayana, 2012). Complications arising from the processing of NC metals, such as the introduction of artifacts (Guduru et al., 2007), have been cited as a major limitation of ductility in this class of materials (Koch, 2003). The post-yielding behavior of NCs has been shown to be quite sensitive to the chosen processing route with it being possible to optimize the process parameters, and therefore the microstructure, to achieve maximum strength and ductility for a given mechanical processing route. To this end, the influence of the initial dislocation density, a direct result of processing, on the ductility of NC Cu is explored in the limit of dislocation-mediated plasticity via the current model. A normal distribution polycrystalline aggregate is simulated over the nanometer range (i.e., grain sizes of 5, 7, 10, 14, 22, 32, 51, and 118 nm) using the two initial dislocation densities utilized in Section 4.3. The boundary conditions described in Section 4.1 are maintained, however, the direction of velocity applied to the top $x-y$ face is along the $+z$ axis direction simulating uniaxial tension at a strain rate of 1×10^{-4} s^{-1}. Since our model does not contain any failure modes, such as cavitation at the grain boundaries (Yujie Wei et al., 2006), the ductility of the simulated microstructures is instead determined via the Considère criterion. In the Considère criterion, the onset of necking (plastic instability in tension) is expected to occur when the value of the strain-hardening rate, $d\sigma/d\epsilon$, equals the value of the true stress, which can be readily computed via an intersection method in MATLAB.

Fig. 8 shows the distribution of the yield stress of the simulated NC Cu aggregates of varying grain size and initial dislocation density normalized by the yield stress of coarse-grained Cu (~80 MPa) as a function of the % elongation to necking, compared to experimental data referenced from Zhu and Liao (2004). In general, it can be seen that the NC Cu simulated in this study falls well within the experimental data range of high strength, but low ductility (i.e., left side of observed bound line), despite changes in the initial dislocation density (see Fig. 8(b)). For the cases with the calibrated initial dislocation density (closed markers), the normalized yield stress increases with decreasing grain size, expectedly, however, at grain sizes above ~32 nm, a decrease in % elongation is observed. An inverse of this trend is observed for the increased initial dislocation density cases (open markers) where a decrease in % elongation is observed as the grain size is reduced below ~32 nm. Note that regions of relatively constant % elongation are

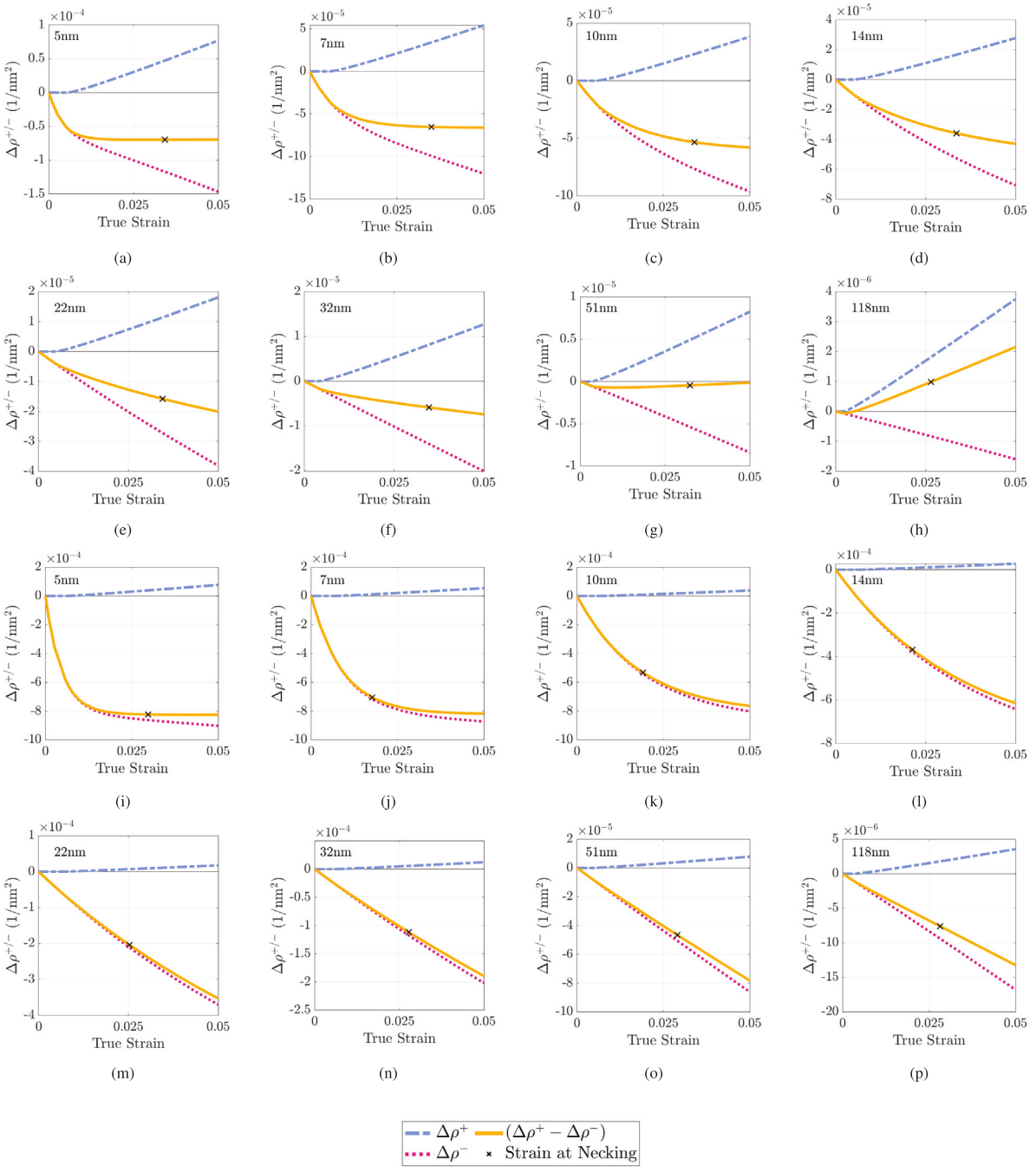

Fig. 9. Evolution of the bulk-averaged change in dislocation density with strain showing the accumulated changes in nucleation, $(\Delta\rho^{+})$, and absorption, $(\Delta\rho^{-})$, along with their difference, $(\Delta\rho^{+} - \Delta\rho^{-})$, as a function of grain size and initial dislocation density. Note that the changes displayed here are relative to the initial dislocation density (now the zero line). Subfigures (a-h) show the evolution of ρ for the calibrated value of ρ_0 for the 5 nm through 118 nm grain sizes, respectively. Subfigures (i-p) show the evolution of ρ for the increased value of ρ_0 for the 5 nm through 118 nm grain sizes, respectively. In all subfigures, the strain at necking has been denoted with a black cross marker.

observed in both dislocation density conditions. As the only free parameter here is the dislocation density, this observed variation in trend must be related to the evolution of the nucleation and absorption rates of dislocation density in the NCs leading to grain size regions where one rate dominates.

Fig. 9 shows the evolution of the bulk-averaged change in dislocation density along with its nucleation and absorption components as a function of strain for varying grain sizes and initial dislocation density values. As noted previously, the % elongation

for the cases with the calibrated value of ρ_0 decreased for grain sizes below 32 nm (see Fig. 9(g–h)) and inversely for the cases with the increased value of ρ_0 showed a decrease in % elongation for grain sizes above 32 nm (see Fig. 9(i–m)). It is found that for the calibrated value of ρ_0, as the grain size is reduced the evolution of the change in dislocation density transitions from a regime dominated by the nucleation rate resulting in a positive net change in $\Delta\rho$ to one dominated by the absorption rate such that the net change in $\Delta\rho$ approaches a negative saturation value. The decreased dislocation density with increasing strain diminishes the strain hardening rate, resulting in the early onset of plastic instability. Similarly, when the initial dislocation density is increased, as the grain size is reduced, the evolution of the change in dislocation density stays absorption rate dominated across all grain sizes, however, the evolution of $\Delta\rho$ transitions from a monotonic behavior to a one where the negative net change in $\Delta\rho$ becomes saturated due to the balance of the nucleation and absorption rate terms. In almost all cases, the net change in $\Delta\rho$ is negative meaning that the total dislocation density in the material is being reduced with strain, i.e., the absorption rate is generally dominant for the bulk nanocrystalline Cu studied here. Despite this, the sensitivity of the deformation response to the initial microstructural state, for a fixed grain size distribution shape, suggests that potential avenues for optimizing the processing parameters to maximize ductility can be guided by simulated efforts by tuning specific model parameters such as those related to the diffusivity of the grain boundaries, which is inherently tied to the processing route. Further, the sensitivity of the model predictions to the grain size implies that other microstructural strategies, such as tailoring the processing to produce a wide grain size distribution or even a bimodal one, may be effective in increasing the ductility of bulk NC metals (Koch, 2003).

4.6. Influence of initial dislocation density and GB diffusivity on post-yielding behavior

It is expected that processing will impact the structure of the GBs in the NC, in addition to the morphology of the microstructure and dislocation density, and will thus affect the diffusivity of the GBs (Hao et al., 2020). NCs, particularly those produced by SPD methods, are susceptible to the formation of higher energy, non-equilibrium GBs that contain an excess dislocation content and atomic disorder (Vetterick et al., 2017) which may improve their capacity as sinks. To explore the influence that the processing state has on the bulk deformation behavior of NCs post-yielding, as predicted by the model, the GB diffusivity, D_{gb}, is systematically varied along with the initial dislocation density, ρ_0, from the calibrated values in Table 1. An initial processing state of the NC is represented by a unique pairing of D_{gb} and ρ_0 here. Values of D_{gb} (8×10^{-2}, 8×10^{-3}, 8×10^{-4} nm^2/s) are chosen to capture the range of experimentally reported values of high purity coarse-grained Cu from Surholt and Herzig (1997). Similarly, the two values of initial dislocation density from Section 4.3 are utilized which effectively bound the experimentally reported range of post-processing dislocation densities in NCs. As it has been previously shown that the shape of the grain size distribution has minimal effect on observed macroscopic trends in the data, the results here focus on only the normal grain size distribution shape for clarity.

Fig. 10(a–h) shows the variation in the stress–strain responses of polycrystalline aggregates with a normal grain size distribution shape of eight grain sizes (5, 7, 10, 14, 22, 32, 51, and 118 nm) as D_{gb} and ρ_0 are increased from their calibrated values. It is found that, for the 118 nm case, increasing D_{gb} to 8×10^{-3} nm^2/s results in a minor decrease in the strain-hardening rate while still retaining similar yield strength to the calibrated case and near to perfect-plastic flow behavior post-yielding. The upper limit case where $D_{gb} = 8\times10^{-2}$ nm^2/s, however, exhibits both a lower yield strength and a notable strain-softening behavior post-yield, the latter of which has been experimentally observed in NCs produced via SPD methods (Haouaoui et al., 2004). As the grain size is reduced towards 22 nm, this observation remains relatively consistent, however, reducing the grain size below 22 nm results in the stress–strain responses transitioning to a mild bulk strain-hardening behavior with the strengths becoming comparable or overlapping.

Fig. 10(i–p) shows the corresponding variations in the dislocation density evolution as D_{gb} is increased, thereby solely affecting the absorption rate of GB dislocations per Eq. (17). It is noted here that the calibrated case shows an initial decrease of dislocation density throughout loading in the elastic regime followed by a monotonic increase as early plasticity develops, agreeing qualitatively with the experimental observations of Adachi et al. (2016), supporting the assumption of diffusive processes dominating dislocation absorption in dislocation-mediated plasticity of NCs. The 118 nm grain size with $D_{gb} = 8\times10^{-2}$ nm^2/s exhibits a near order of magnitude decrease in dislocation density by 5% strain contributing to a decrease in the athermal strengthening from dislocation density by 57.3 MPa (or 58%) from the initial value of 98.41 MPa, producing the observed strain-softening response as the deformation proceeds. As the grain size is reduced towards 22 nm, the evolution of the dislocation density for the cases where $D_{gb} = 8\times10^{-2}$ nm^2/s rapidly approaches a saturation value, however, reducing below 22 nm results in an "overshoot" like behavior where the initial absorption rate is extremely high reducing the athermal strengthening prior to yielding the promptly establishing a steady-state value of ρ as plastic deformation begins. This trend is also observed for the cases where $D_{gb} = 8\times10^{-3}$ nm^2/s while the cases of $D_{gb} = 8\times10^{-4}$ nm^2/s maintain a smooth transition from absorption to a steady-state condition.

Fig. 11 shows the strain-hardening rate, $\theta = d\sigma/d\epsilon$, sampled at 5% strain Khan et al. (2008) as a function of D_{gb} for eight average grain sizes (5, 7, 10, 14, 22, 32, 51, and 118 nm) simulated at the two initial dislocation densities utilized in Section 4.3. It is found that θ exhibits two differing trends in its evolution as a function of D_{gb} and $\overline{d}$, noting that the initial dislocation density seems to generally impact only the magnitude of θ and not the qualitative trends. Focusing on the larger grain sizes, while the 118 nm cases show a transition from mild strain-hardening to strain-softening as D_{gb} increases, this is not observed as $\overline{d}$ is decreased. Both the 32 nm and 51 nm cases transition to a perfect-plastic or strain-softening behavior as D_{gb} is increased to 8×10^{-3} nm^2/s, however, increasing further to 8×10^{-2} nm^2/s recovers similar mild strain-hardening behaviors observed for the calibrated value of D_{gb}. This observed shift in the evolution of θ as D_{gb} is increased in reduced grain sizes is caused by the resulting variations in dislocation density evolution which influences both the magnitude of dislocation density and rate of dislocation storage measured at 5% strain. Considering the cases where $\rho_0 = 9.3\times10^{-4}$ nm^{-2} for comparison, when $D_{gb} = 8\times10^{-4}$ nm^2/s both the 32 nm and 51 nm grain sizes

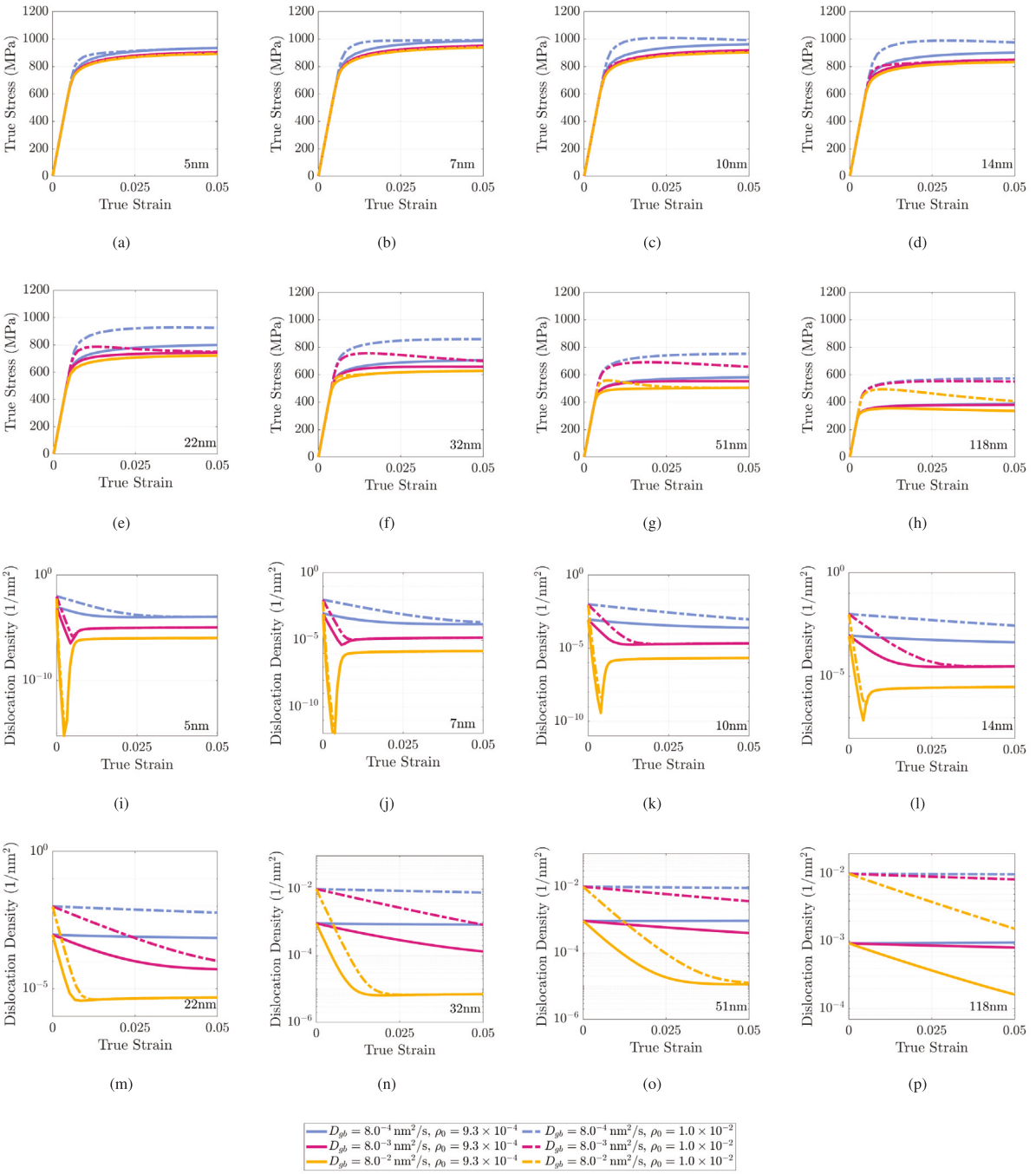

Fig. 10. Simulated results obtained for a polycrystalline aggregate with a normal grain size distribution shape where grain size, $\bar{d}$, is varied. (a-h) Simulated true stress–strain responses showing the variation of GB diffusivity and initial dislocation density inducing different macroscopic strain hardening or softening behaviors at grain sizes of 5, 7, 10, 14, 22, 32, 51, and 118 nm, respectively. (b) Evolution of the bulk-averaged dislocation density as a function of strain showing the influence of GB diffusivity and initial dislocation density on the rates of dislocation storage at grain sizes of 5, 7, 10, 14, 22, 32, 51, and 118 nm, respectively.

exhibit only minor variations in ρ at 5% strain compared to ρ_0 with a 8.5% decrease and 0.26% increase observed, respectively. As D_{gb} is increased to 8×10^{-3} nm^2/s, the rate of dislocation absorption results in a near order of magnitude decrease in the dislocation density maintaining a negative rate of dislocation storage with $\partial\rho/\partial\epsilon$ at 5% strain being -0.0031 nm^2 and -0.0057 nm^2 for the 32 nm and 51 nm grain sizes, respectively. At the highest D_{gb} of 8×10^{-2} nm^2/s, both grain sizes show a significantly increased absorption rate during the elastic regime with the dislocation density magnitude decreasing nearly two orders of magnitude and

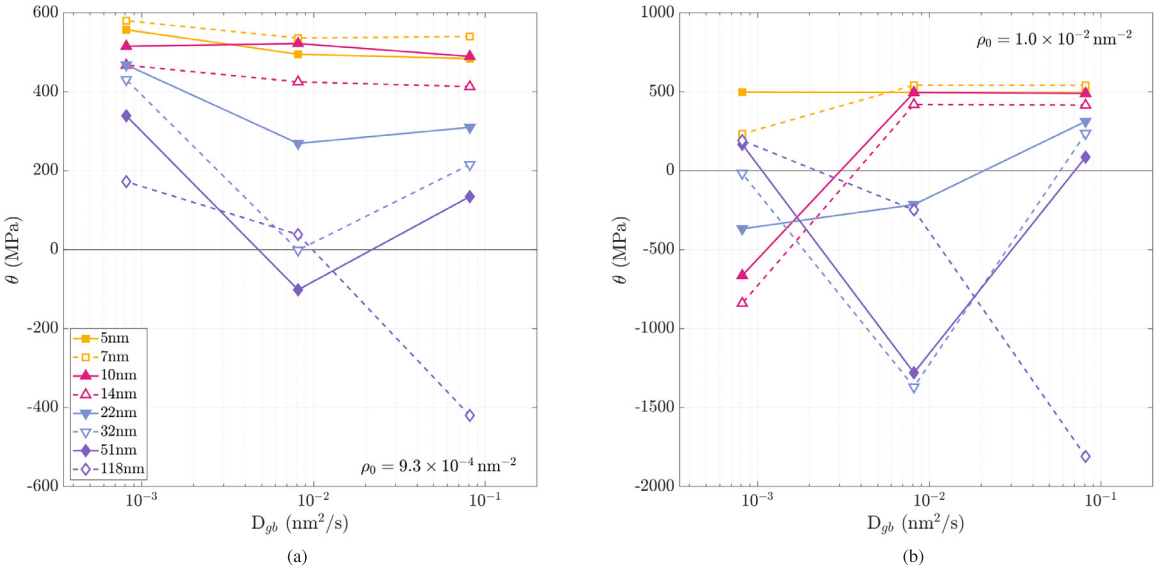

Fig. 11. Simulated variation in the strain hardening rate, θ, measured at 5% strain as a function of GB diffusivity for NC Cu with various average grain sizes, $\bar{d}$, and initial dislocation densities, ρ_0. (a) Variation in strain hardening rate for the calibrated value of initial dislocation density. (b) Variation in strain hardening rate for the increased value of initial dislocation density. The respective initial dislocation densities utilized are inset into the subfigures.

reaching saturation before 5% strain, leading to the observed recovery in the macroscopic strain-hardening. This exploration reveals the sensitivity of the post-yielding behaviors of NCs to the rate of dislocation absorption which is related to the structure (or disorder) of the GBs, which will vary from different processing methods. Although the present model employs a limiting assumption in the grain-uniform plasticity, the effect of varying the GB diffusivity is notable on the deformation response post-yielding, especially when combined with an increased initial dislocation density. It is expected that a model accounting for the influence of various microstructural effects on the GB diffusivity, such as slip continuity across the GB interface (Wang et al., 2017; Fressengeas and Upadhyay, 2020), would work towards resolving the development of deformation patterning resulting from dislocation-mediated plasticity in NCs.

5. Conclusions

A dislocation-density-based crystal plasticity model for NC FCC metals based on a thermally-activated dislocation depinning mechanism was developed. The constitutive equations for classical crystal plasticity were reformulated to account for the nucleation-propagation-absorption process of dislocations proposed for NCs with a simple KME-type dislocation kinetics model introduced to account for the dislocation density evolution at the GB. In particular, the model was formulated independently of any additional GB-mediated plastic deformation mechanisms facilitating the exploration of the fundamental role of dislocation-mediated plasticity in the deformation of NCs. The proposed constitutive model was implemented into ABAQUS using a user subroutine UMAT to perform full-field crystal plasticity simulations of bulk aggregates and to study the influence of the initial microstructure and processing state on the mechanical performance of NC Cu. Experimental measurements on the bulk compression of NC Cu, accounting for various average grain sizes and strain rates, were used to calibrate the material-specific model parameters.

The modeling effort presented in this work builds upon the well-established mechanistic description of dislocation motion as a thermally-activated process. As such, the present scope is to provide a more complete understanding of the structure-processing-property relationship for nanocrystalline metals whose deformation is still dominated by dislocation activity (e.g., larger grain sizes within the nanometer range). This is achieved by establishing a dislocation-density-based crystal plasticity model whose constitutive equations appropriately represent the physically established "nucleation–propagation–absorption" process of dislocation behavior in nanocrystalline metals and exploring the impact of the initial microstructural state on the yielding and post-yielding behaviors of nanocrystalline metals that have been prepared/processed in various ways. Of particular importance to the current work is the description of the grain boundaries as both sources and sinks for dislocations and the accounting for the nucleation and absorption processes at the GBs explicitly through the construction of the dislocation density evolution equations. Further, by omitting other potentially competing deformation mechanisms, the model presented here is capable of probing the functional limits where dislocation-mediated plasticity is no longer expected to dominate the overall plastic deformation response.

The proposed constitutive model successfully reproduced the experimental trend of yield strength as grain size is reduced, with the variation in grain size distribution shape and initial dislocation density contributing to a wide variation in strength capturing the experimental scatter well. An inverse Hall–Petch effect was observed for grain sizes below 7 nm due to a combined influence from a drop off in peak grain size athermal strengthening and a reduction in athermal strengthening from the dislocation density due to

increased absorption rates. The increased strain rate-sensitivity of NC Cu was captured, however, only a weak positive correlation with grain size was observed supposed to the lack of GB-mediated plastic deformation mechanisms with notable deviation from experimental data observed. It was found that increasing the initial dislocation density of the material led to a minor decrease in ductility (% elongation), coinciding with an increase in yield strength of the material, expectedly, but despite this, the behavior of the nanocrystalline Cu simulated here aligns well with the high strength and low ductility expectation for NCs from experimental literature. An increase in the initial dislocation density is found to increase the yield strength and notably amplifies the strain-hardening (or softening) rates of the NC post-yielding. Lastly, it is found that variation in the GB diffusivity also greatly impacts the post-yielding response in conjunction with both the average grain size and initial dislocation density. This exemplifies the capability of the developed model to investigate the mechanical performance of complexion-engineered NCs (Turlo and Rupert, 2018).

With the successful implementation of the dislocation-mediated constitutive model, other proposed NC deformation mechanisms, particularly those directly involving the GBs, may be re-incorporated in a systematic manner. This will work to resolve the competition between dislocation- and GB-mediated plasticity in NCs by introducing the additional mechanisms consistently into the proposed kinematic framework (Taupin et al., 2015). The crystal plasticity model presented here may also be used to develop a dual-phase microscale model accounting for the interactions of dislocations with amorphous-crystalline interfaces in novel nanostructured composite materials by coupling the present model with another finite element-based framework, such as the shear transformation zone dynamics model, to simulate the plastic deformation of amorphous or glass-like regions in the dual-phase microstructure (Gu et al., 2023).

CRediT authorship contribution statement

Jonathan Cappola: Writing – original draft, Visualization, Validation, Software, Methodology, Investigation, Formal analysis, Data curation. **Jian Wang:** Writing – review & editing, Resources, Investigation, Funding acquisition, Formal analysis, Conceptualization. **Lin Li:** Writing – review & editing, Supervision, Resources, Project administration, Investigation, Funding acquisition, Formal analysis, Conceptualization.

Declaration of competing interest

The authors declare no conflict of interest.

Data availability

Data will be made available on request.

Acknowledgments

All authors would like to acknowledge the support of NSF-CMMI-2331482/2132336. JC acknowledges financial support from the Alabama Graduate Research Scholars Program (GRSP) funded through the Alabama Commission for Higher Education and administered by the Alabama EPSCoR, United States of America (NSF-CMMI-1727875). The authors acknowledge Research Computing at Arizona State University for providing HPC resources that have contributed to the research results reported within this paper. We thank the reviewers for their time spent on careful reviewing of our manuscript and for their insightful comments and suggestions that improved the quality of the manuscript.

Appendix A. Grain-level computational procedure

At the start of an increment at time t in UEXTERNALDB (i.e., prior to the call to UMAT and the solving of the constitutive equations), the total deformation gradient at each ith IP at the end of the increment for time $\tau = t + \Delta t$, $\mathbf{F}_i(\tau)$, is computed using estimate of the velocity gradient, $\mathbf{L}_i(\tau)$, from the previous iteration, defined in Eq. (B.4), and the total deformation gradient, $\mathbf{F}_i(t)$, obtained from the previous increment per McKenzie (1979) as

$$\mathbf{F}_i(\tau) = \left[\mathbf{I} - \frac{\Delta t}{2}\mathbf{L}_i(\tau)\right]^{-1}\left[\mathbf{I} + \frac{\Delta t}{2}\mathbf{L}_i(\tau)\right] \cdot \mathbf{F}_i(t). \tag{A.1}$$

Within the UMAT, the computational procedure begins by volume-averaging the total deformation gradient at time τ for the gth grain, $\overline{\mathbf{F}}_g(\tau)$, as

$$\overline{\mathbf{F}}_g(\tau) = \frac{1}{V_g}\sum_i \left(\det \mathbf{F}_i(\tau)\right) V_i \mathbf{F}_i(\tau), \tag{A.2}$$

where V_i is the volume of the ith IP within the gth grain in the reference configuration (i.e., $t = 0$) and, here, V_g is the volume of the grain relative to the dimensions of the finite element mesh. Note that the summation in Eq. (A.2) takes place over the set of IPs that belong to the set of elements assigned to the gth grain in the element-to-grain index input file. With $\overline{\mathbf{F}}_g(\tau)$ now calculated

and $\overline{\mathbf{F}}_g^{\mathrm{p}^{-T}}(t)$ known from the previous increment, the solution proceeds as usual following the time-integration scheme of Kalidindi et al. (1992). The grain-volume-averaged elastic stress at time τ is obtained as

$$\overline{\mathbf{T}}_g^{\mathrm{e}}(\tau) \approx \overline{\mathbf{T}}_g^{\mathrm{e,tr}} - \sum_\alpha \Delta\gamma_g^\alpha \mathbf{C}^\alpha \tag{A.3}$$

where $\overline{\mathbf{T}}_g^{\mathrm{e,tr}}$ is the grain-volume-averaged elastic trial stress

$$\overline{\mathbf{T}}_g^{\mathrm{e,tr}} = \boldsymbol{\mathcal{C}}\left[\frac{1}{2}\left(\mathbf{A}-\mathbf{I}\right)\right], \tag{A.4}$$

with

$$\mathbf{C}^\alpha \equiv \boldsymbol{\mathcal{C}}\left[\frac{1}{2}\left\{\mathbf{A}\mathbf{S}_0^\alpha + \mathbf{S}_0^{\alpha^T}\mathbf{A}\right\}\right], \tag{A.5}$$

and

$$\mathbf{A} \equiv \overline{\mathbf{F}}_g^{\mathrm{p}^{-T}}(t)\,\overline{\mathbf{F}}_g^{T}(\tau)\,\overline{\mathbf{F}}_g(\tau)\,\overline{\mathbf{F}}_g^{\mathrm{p}^{-1}}(t), \tag{A.6}$$

while $\Delta\gamma_g^\alpha$ is a scalar function of the unknown terms $\overline{\mathbf{T}}_g^{\mathrm{e}}(\tau)$ and $s_{ath}^\alpha(\tau)$ given by

$$\Delta\gamma_g^\alpha \equiv \dot{\gamma}_g^\alpha\left(\overline{\mathbf{T}}_g^{\mathrm{e}}(\tau), s_{ath}^\alpha(\tau)\right)\cdot\Delta t. \tag{A.7}$$

By substituting Eq. (A.7) into Eq. (A.3), a set of non-linear equations in terms of the unknowns is obtained which is solved using a two level Newton–Raphson iterative scheme by the following equations:

$$\overline{\mathbf{T}}_{g,n+1}^{\mathrm{e}}(\tau) = \overline{\mathbf{T}}_{g,n}^{\mathrm{e}}(\tau) - \mathcal{J}_n^{-1}\left[\mathbf{G}_n\right], \tag{A.8}$$

$$\mathbf{G}_n \equiv \overline{\mathbf{T}}_{g,n}^{\mathrm{e}}(\tau) - \overline{\mathbf{T}}_g^{\mathrm{e,tr}} + \sum_\alpha \Delta\gamma_g^\alpha\left(\overline{\mathbf{T}}_{g,n}^{\mathrm{e}}(\tau), \left(s_{ath}^\alpha(\tau)\right)_k\right)\mathbf{C}^\alpha, \tag{A.9}$$

where

$$\mathcal{J}_n \equiv \mathbf{I} + \sum_\alpha \mathbf{C}^\alpha \otimes \frac{\partial\Delta\gamma_g^\alpha\left(\overline{\mathbf{T}}_{g,n}^{\mathrm{e}}(\tau), \left(s_{ath}^\alpha(\tau)\right)_k\right)}{\partial\overline{\mathbf{T}}_{g,n}^{\mathrm{e}}(\tau)}. \tag{A.10}$$

In Eq. (A.8)–(A.10), the subscript n denotes the nth iteration of the first level of the iterative scheme, where s_{ath}^α is fixed at the best available estimate, and the subscript k denotes the kth update (without iteration) of s_{ath}^α in the second level of the iterative scheme after $n+1$ iterations. As the evolution of s_{ath}^α is only dependent on the evolution of ρ^α through $s_{ath,\rho}^\alpha$, following Alankar et al. (2009), it is assumed that $\rho_k^\alpha(\tau)$ remains constant while determining $\mathcal{J}_n$ as

$$\frac{\partial\Delta\gamma_g^\alpha\left(\overline{\mathbf{T}}_{g,n}^{\mathrm{e}}(\tau), \rho_k^\alpha(\tau)\right)}{\partial\overline{\mathbf{T}}_{g,n}^{\mathrm{e}}(\tau)} = \rho_k^\alpha(\tau)\frac{\partial\Delta\gamma_g^\alpha\left(\overline{\mathbf{T}}_{g,n}^{\mathrm{e}}(\tau)\right)}{\partial\overline{\mathbf{T}}_{g,n}^{\mathrm{e}}(\tau)}. \tag{A.11}$$

The dislocation densities are updated using Eq. (17) as

$$\rho_{k+1}^\alpha(\tau) = \rho^\alpha(t) + \left(\dot{\rho}_k^\alpha(\tau)\right)\cdot\Delta t, \tag{A.12}$$

and, subsequently, the athermal strength contributions (Eq. (12)) from the dislocation densities by

$$\left(s_{ath,\rho}^\alpha\right)_{k+1}(\tau) = \alpha\mu b\sqrt{\rho_{k+1}^\alpha(\tau)}, \tag{A.13}$$

noting that the athermal strength contribution from the grain size does not evolve in the present model. The two level iterative scheme proceeds until the L_2 norm of the incremental changes in $\overline{\mathbf{T}}_g^{\mathrm{e}}(\tau)$ and $s_{ath,\rho}^\alpha(\tau)$ satisfies the required tolerances of 10^{-4} and 10^{-3}, respectively. Note that incremental changes in the slip resistances are monitored instead of the dislocation densities due to the exponential growth of the latter potentially causing numerical stability issues (Ha et al., 2017). Once both levels of the iterative scheme are fully converged and $\Delta\gamma_g^\alpha$ is known, the evolution of the grain-uniform plastic deformation gradient is obtained with Eqs. (4) and (5) using an approximation of the exponential map as

$$\overline{\mathbf{F}}_g^{\mathrm{p}}(\tau) \approx \left\{\mathbf{I} + \sum_\alpha \Delta\gamma_g^\alpha \mathbf{S}_0^\alpha\right\}\overline{\mathbf{F}}_g^{\mathrm{p}}(t), \tag{A.14}$$

where it is necessary to normalize $\overline{\mathbf{F}}_g^{p}(\tau)$ by dividing by the cube root of $\det\left(\overline{\mathbf{F}}_g^{p}(\tau)\right)$ to maintain plastic incompressibility. Note that the converged result of $\overline{\mathbf{T}}_g^{\mathrm{e}}(\tau)$ is discarded here as it is only necessary to determine $\Delta\gamma_g^\alpha$ for the grain-uniform plastic deformation. The grain-uniform accumulated plastic shear strain at the end of the increment, $\gamma_g^\alpha(\tau) = \gamma_g^\alpha(t) + \Delta\gamma_g^\alpha$, is then updated along with various grain-level storage arrays from the MODULE, all of which is performed within a MUTEXLOCK. The texture at time τ can be computed following Kalidindi et al. (1992), however, as the influence of texture is outside of the present scope, the equations are omitted for brevity. At this point, the grain-level solution for homogeneous plastic deformation has completed and the successful grain-level solution for the gth grain is flagged in the associated global logical array.

Appendix B. Integration-point-level computational procedure

Once the grain-level solution for the gth grain has been completed, irrespective of the solution was provided by the ith IP, the local Cauchy stress and material Jacobian matrix must be returned to ABAQUS at each IP within the finite element mesh. Since $\overline{\mathbf{F}}_g^p(\tau)$ has been previously obtained, the local Cauchy stress state, $\boldsymbol{\sigma}_i(\tau)$, at the ith IP can be computed explicitly as

$$\boldsymbol{\sigma}_i(\tau) = \frac{1}{\det \mathbf{F}_i^{\mathrm{e}}(\tau)} \cdot \mathbf{F}_i^{\mathrm{e}}(\tau) \cdot \mathbf{T}_i^{\mathrm{e}}(\tau) \cdot \mathbf{F}_i^{\mathrm{e}^{\mathrm{T}}}(\tau), \tag{B.1}$$

where

$$\mathbf{F}_i^{\mathrm{e}}(\tau) = \mathbf{F}_i(\tau) \overline{\mathbf{F}}_g^{\mathrm{p}^{-1}}(\tau). \tag{B.2}$$

and $\mathbf{T}_i^{\mathrm{e}}(\tau)$ is computed by the insertion of Eq. (B.2) into Eqs. (2) and (3). The computation of the analytical material Jacobian matrix, denoted as $\mathcal{W}(\tau)$, follows that of Balasubramanian (1998), with minor modifications due to the assumption of grain-uniform plasticity, as

$$\mathcal{W}(\tau) \equiv \frac{\partial \boldsymbol{\sigma}(\tau)}{\partial \mathbf{E}_t(\tau)}, \tag{B.3}$$

where the i subscript on the Cauchy stress is dropped and $\mathbf{E}_t(\tau)$ is the symmetric relative strain tensor, defined later. Here, the relative deformation gradient, $\mathbf{F}_t(\tau)$, is given as $\mathbf{F}_t(\tau) = \mathbf{F}(\tau)\mathbf{F}^{-1}(t)$. The polar decomposition of this relative deformation gradient, $\mathbf{F}_t(\tau) = \mathbf{R}_t(\tau)\mathbf{U}_t(\tau)$, thus results in the relative rotation tensor, $\mathbf{R}_t(\tau)$, and the relative stretch tensor, $\mathbf{U}_t(\tau)$, from which $\mathbf{E}_t(\tau)$ can be obtained as $\ln \mathbf{U}_t(\tau)$. For a small incremental stretch, the approximation $\mathrm{d}\mathbf{E}_t(\tau) \approx \mathrm{d}\mathbf{U}_t(\tau)$ simplifies the derivation of $\mathcal{W}(\tau)$ to $\partial\boldsymbol{\sigma}(\tau)/\partial\mathbf{U}_t(\tau)$. The algorithm to compute the Jacobian expressed in index notation follows directly:

1. $\mathcal{L}_{ijkl} = F_{ik}^{e^T}(t)\, U_{t,lm}(\tau)\, F_{mj}^{e}(t) + F_{im}^{e^T}(t)\, U_{t,mk}(\tau)\, F_{lj}^{e}(t)$
2. $\mathcal{D}_{ijkl} = \frac{1}{2} C_{ijmn} \mathcal{L}_{mnkl}$
3. $\mathcal{G}_{mnkl}^{\alpha} = \mathcal{L}_{mpkl} \mathrm{S}_{0,pn}^{\alpha} + \mathrm{S}_{0,mp}^{\alpha^T} \mathcal{L}_{pnkl}$
4. $\mathcal{J}_{ijkl}^{\alpha} = \frac{1}{2} C_{ijmn} \mathcal{G}_{mnkl}^{\alpha}$

Here, the decoupling of $\dot{\gamma}_g^{\alpha}$ from the local IP's stress state allows for a minor simplification of the remaining terms, as the associated partial derivative $\partial \Delta\gamma_g^{\alpha}(\tau)/\partial \mathbf{T}_i^{e}(\tau)$ becomes zero (cf. Eq. B.38 in Balasubramanian (1998)).

5. $\mathcal{Q}_{ijkl} = \mathcal{D}_{ijkl} - \sum_{\alpha} \Delta\gamma_g^{\alpha}(\tau)\, \mathcal{J}_{ijkl}^{\alpha}$
6. $\mathcal{S}_{ijkl} = R_{t,ik} F_{ij}^{e}(t) - R_{t,ik} F_{ip}^{e}(t) \sum_{\alpha} \Delta\gamma_g^{\alpha}(\tau)\, \mathrm{S}_{0,pj}^{\alpha}$
7. $\mathcal{W}_{ijkl} = \frac{1}{\det \mathbf{F}^{\mathrm{e}}} \left[\mathcal{S}_{imkl} T_{mn}^{e}(\tau) F_{nj}^{e^T}(\tau) + F_{im}^{e}(\tau) \mathcal{Q}_{mnkl} F_{nj}^{e^T}(\tau) + F_{im}^{e}(\tau) T_{mn}^{e}(\tau) \mathcal{S}_{jnkl} - F_{im}^{e}(\tau) T_{mn}^{e}(\tau) F_{nj}^{e^T}(\tau) \left(S_{pqkl} F_{qp}^{e^{-1}}(\tau) \right) \right]$

Above, several tensor terms defined earlier in Section 2 are utilized in their respective index notation forms. These include F_{ij}^{e}, C_{ijkl}, $\mathrm{S}_{0,ij}^{\alpha}$, and T_{ij}^{e}, which are simply $\mathbf{F}^{\mathrm{e}}$, $\boldsymbol{C}$, $\mathbf{S}_0^{\alpha}$, and $\mathbf{T}^{\mathrm{e}}$, respectively, from Eqs. (1), (2), and (7). $\mathcal{W}_{ijkl}$ is then reduced to the $\mathcal{W}_{ij}$ form as expected by ABAQUS (cf. Eq. B.8 in Balasubramanian (1998)). It is noted that the derived Jacobian here lacks major symmetry and as such the UNSYMM option available in ABAQUS in enabled during simulation. The piecewise form of Eq. (11) does not pose any complications to the evaluation of the Jacobian as presented here. The shearing rate is computed at the grain-level, as denoted by the use of $\Delta\gamma_g^{\alpha}(\tau)$, and is only used to evolve of the grain-uniform plastic deformation gradient across the time increment (cf. Eq. (A.14)), which in turn, affects the resulting local elastic deformation gradient obtained via Eq. (B.2). If a particular slip system is inactive (i.e., Eq. (11) returns zero), then its contribution to the summation term in Eq. (A.14) is simply zero as well and does not contribute to the evolution of $\overline{\mathbf{F}}_g^{\mathrm{p}}$. In the event that all slip systems are inactive, such as during purely elastic loading, then $\overline{\mathbf{F}}_g^{\mathrm{p}}$ does not evolve over the time increment and $\Delta\gamma_g^{\alpha}$ is zero for all slip systems, thus the computations of Step 5 and 6 simplify down, eliminating the negative terms on the right hand sides. To close the IP-level computation, any desired output state variables are stored into the STATEV array provided by ABAQUS and the velocity gradient at the end of the increment is estimated as

$$\mathbf{L}_i(\tau) \approx \left(\frac{\mathbf{F}_i(\tau) - \mathbf{F}_i(t)}{\Delta t} \right) \cdot \mathbf{F}_i^{-1}(\tau) \tag{B.4}$$

which is recomputed for each IP at each iteration within an increment to ensure the deformation gradient extrapolations utilized in Eq. (A.1) benefit from corrections made by ABAQUS to the displacement field during iterative convergence of the increment.

Appendix C. Influence of homogenized plastic deformation gradient on slip activity

As discussed in Section 2, a key assumption in the construction of the present nanocrystal plasticity model is that of the homogenization of the plastic deformation gradient across the grain. This produces a "coarse-shearing" effect on plastic deformation that is driven by the grain-volume-averaged elastic stress state. It is reasonable to expect that the assumption of homogeneous plastic deformation across the grain may impact otherwise expected slip activity in the grain due to the inability for elements near to boundaries, for instance, to accommodate the deformation through the local activation of slip systems. Illustrative examples are presented here to provide insight into how this key assumption impacts the development of plasticity.

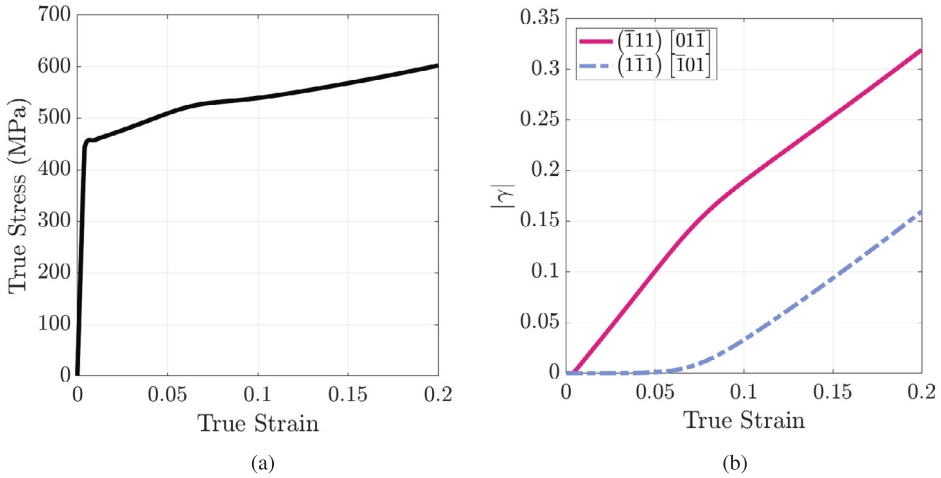

Fig. C.1. (a) Simulated stress–strain response in uniaxial tension for the $\langle\bar{2}\,3\,6\rangle$ oriented single crystal. (b) Simulated accumulated plastic shear on the two active slip systems in the single crystal, noting the activation of the $(\bar{1}\,1\,1)[0\,1\,\bar{1}]$ system (single slip) prior to the secondary activation of the $(1\,\bar{1}\,1)[\bar{1}\,0\,1]$ system.

To validate the behavior of the model, a single first-order hexahedral element (C3D8) is treated as a 51 nm grain using the model parameters outlined in Table 1 and is pulled in uniaxial tension at a strain rate of 1×10^{-3} 1/s along the z axis utilizing the same boundary conditions as applied to the polycrystalline aggregates in Section 4. The initial Euler–Bunge angles are set such that the $\langle\bar{2}\,3\,6\rangle$ crystal direction was aligned with the tensile axis as in Anand and Kothari (1996). Fig. C.1(a) shows the true stress–strain behavior of the single crystal deformation. It can be seen that there is a linear hardening region post-yielding where only the $(\bar{1}\,1\,1)[0\,1\,\bar{1}]$ slip system is activated followed by the activation of the second $(1\,\bar{1}\,1)[\bar{1}\,0\,1]$ slip system at a strain of approximately 0.07. This can also be seen directly in Fig. C.1(b) which shows the accumulated plastic strain, $|\gamma|$, as strain evolves. These results are in qualitative agreement with the simulated results presented in Anand and Kothari (1996), which is expected as the boundary conditions utilized result in a homogeneous stress state across the single element crystal meaning that the plastic deformation is likewise homogeneous in this case. Thus, the behavior of the model reaches parity with conventional crystal plasticity models in the limit where a single crystal (although not necessarily a single element) is being deformed homogeneously. Further, Fig. C.1(b) highlights that the activation of simultaneous slip systems is still allowed in the present model (i.e., no restrictions on slip system activation is made). Due to the observed lack of dislocation storage at room temperature deformation, it is reasonable to suggest that intragranular dislocation–dislocation interaction during deformation is minimal, hence the lack of any latent hardening behavior in the square root term of Eq. (12) as the interaction is instead with forest-like dislocations within the GB, and thus simultaneous slip systems may be active as the dislocations are expected to propagate across the nanograin interior at rates where interaction can be avoided.

To highlight the variation in the plastic deformation behavior of the present model when compared to conventional crystal plasticity, bicrystal prisms (1:4:1 domain edge length ratio) are tessellated and meshed using second-order tetrahedral elements (C3D10, 1402 elements) assuming both crystals were 51 nm grains. The bottom $x-z$ face is fully constrained while the top $x-z$ face is pulled at a strain rate of 1×10^{-3} 1/s in the y direction. The initial Euler–Bunge angles for each grain are such that either the $\langle\bar{2}\,3\,10\rangle$ or the $\langle0\,6\,7\rangle$ directions are aligned with the tensile axis. Fig. C.2 shows the spatial distribution of von Mises stress and equivalent plastic strain (deformation exaggerated by 5x) for a conventional crystal plasticity model based on the implementation of Kalidindi et al. (1992) and using the material parameters provided in Bronkhorst et al. (1992) for single crystal copper along with predictions of the present nanocrystal plasticity model. It can be seen in Figs. C.2(a) and C.2(b) that the conventional crystal plasticity model predicts localization behavior in the lower single crystal due to the boundary constraints on its deformation, particularly with the fully constrained bottom $x-y$ face leading localized plastic distortion of these elements. The present model with the assumption of homogenized plastic deformation instead predicts no localization and instead the accumulated plastic strain field is (expectedly) constant across each grain (see Fig. C.2(d)) while it can be seen that the von Mises stress is concentrated towards the grain boundary (see Fig. C.2(c)). This is expected since the uniform $\bar{\mathbf{F}}_g^p$ produces a grain-level shape change due to shear, however, compatibility is required to be satisfied. As a result, the elastic stress state throughout the grain is allowed to be heterogeneous and elements near boundaries may distort more in order to maintain compatibility.

This result is echoed in the deformation of the polycrystalline aggregates when deformed in compression, such as for the representative 118 nm polycrystalline aggregate with a normal grain size distribution (the rest of model parameters follow Table 1), where the von Mises stress distribution exhibits higher values near the GBs in the domain, as seen in Fig. C.3(a). This can also be

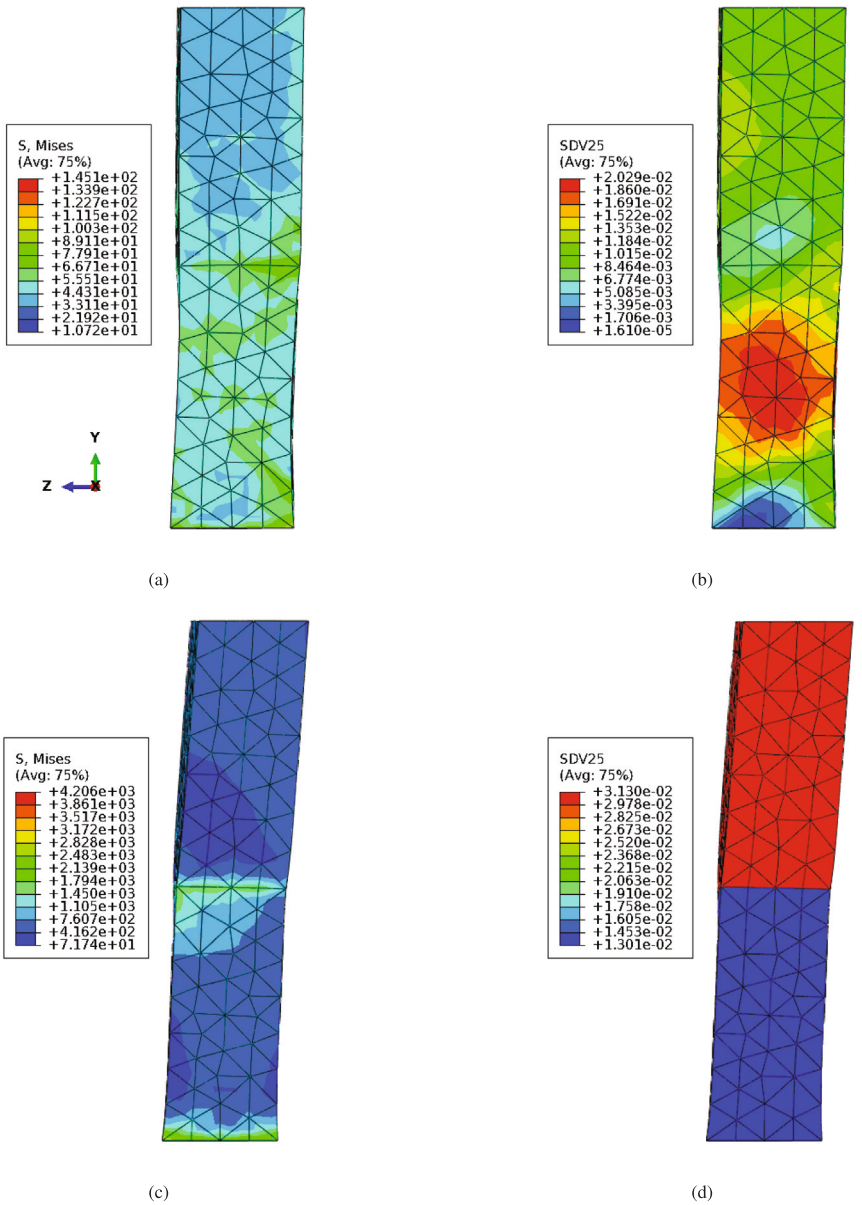

Fig. C.2. Comparison of the spatial distributions in bicrystal prisms of Cu of the von Mises stress (a,c) and the accumulated plastic strain (b,d) sampled after uniaxial tension at a true strain of 0.01 in for (a–b) the conventional crystal plasticity model and (c–d) the nanocrystal plasticity model with grain-uniform plasticity. Deformation is exaggerated by 5x to highlight the differences in displacement between the two models. (For interpretation of the references to color in this figure legend, the reader is referred to the web version of this article.)

seen within the volume if grains are extracted from the polycrystal and sliced such as in Fig. C.3(b) which is the grain at the free surface highlighted in white in Fig. C.3(a). It can be seen that into the volume of the grain, the von Mises stress maintains higher values near to the GBs and approaches an average value towards the centroid. This distribution can also be seen in Fig. C.3(c) which shows the distribution of von Mises stress normalized by grain average values throughout the 118 nm polycrystalline aggregate in the initial condition just after loading begins ($\epsilon \approx 0.0$) and after a strain of 5% is reached. It is noted that the distribution initially displays a normal distribution about unity, while after some plasticity develops, the mean shifts below unity and a wide tail develops on the right side suggesting that elevated elastic strains have developed in the grain near the GBs to maintain compatibility.

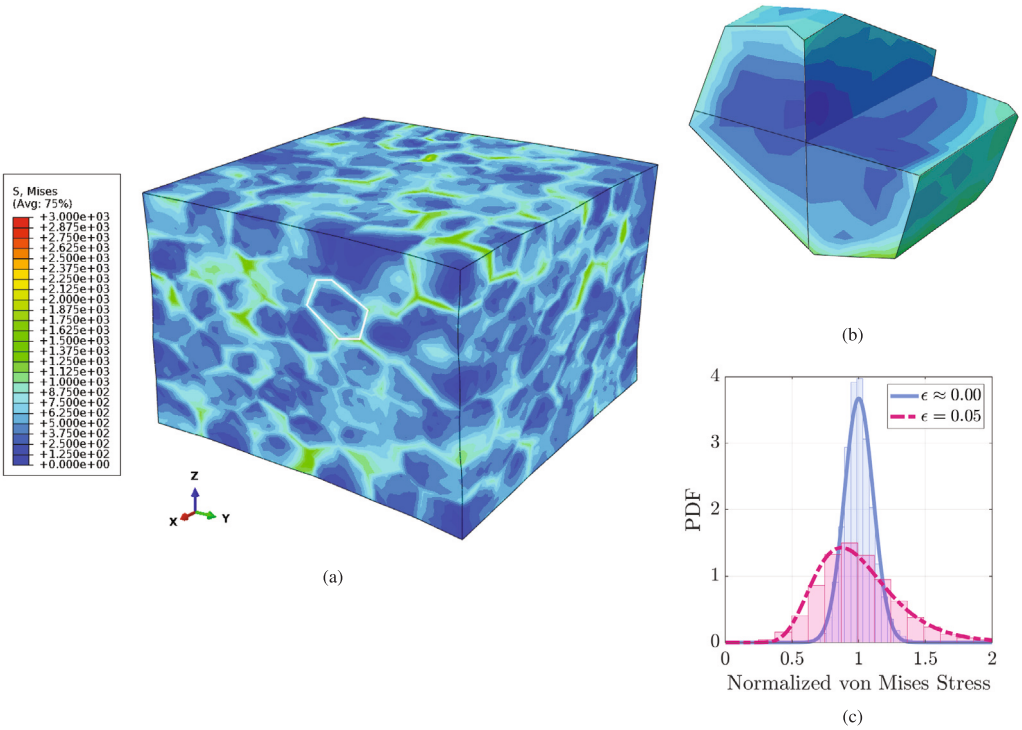

Fig. C.3. (a) von Mises stress distribution on a 118 nm polycrystalline aggregate with a normal grain size distribution after reaching a true strain of 0.05. The grain highlighted on the free surface by the white line in (a) is extracted and the von Mises stress distribution within the grain is shown in (b). (c) The variation in distributions at $\epsilon \approx 0$ and $\epsilon = 5\%$ of the von Mises stresses in the elements of the polycrystalline mesh normalized by their respective grain average von Mises stress. An evolution in this distribution shape after plasticity develops is noted. (For interpretation of the references to color in this figure legend, the reader is referred to the web version of this article.)

References

Adachi, H., Karamatsu, Y., Nakayama, S., Miyazawa, T., Sato, M., Yamasaki, T., 2016. Elastic and plastic deformation behavior studied by In-Situ synchrotron X-ray diffraction in nanocrystalline nickel. Mater. Trans. 57 (9), 1447–1453. http://dx.doi.org/10.2320/matertrans.MH201505.

Alankar, A., Mastorakos, I.N., Field, D.P., 2009. A dislocation-density-based 3D crystal plasticity model for pure aluminum. Acta Mater. 57 (19), 5936–5946. http://dx.doi.org/10.1016/j.actamat.2009.08.028.

Anand, L., Kothari, M., 1996. A computational procedure for rate-independent crystal plasticity. J. Mech. Phys. Solids 44 (4), 525–558. http://dx.doi.org/10.1016/0022-5096(96)00001-4.

Arsenlis, A., Parks, D.M., 2002. Modeling the evolution of crystallographic dislocation density in crystal plasticity. J. Mech. Phys. Solids 50 (9), 1979–2009. http://dx.doi.org/10.1016/S0022-5096(01)00134-X.

Bailey, J.E., Hirsch, P.B., 1960. The dislocation distribution, flow stress, and stored energy in cold-worked polycrystalline silver. Philos. Mag.: J. Theor. Exp. Appl. Phys. 5 (53), 485–497. http://dx.doi.org/10.1080/14786436008238300.

Balasubramanian, S., 1998. Polycrystalline Plasticity: Application to Deformation Processing of Lightweight Metals (Ph.D. thesis). Massachusetts Institute of Technology.

Bitzek, E., Derlet, P., Anderson, P., Van Swygenhoven, H., 2008. The stress–strain response of nanocrystalline metals: A statistical analysis of atomistic simulations. Acta Mater. 56 (17), 4846–4857. http://dx.doi.org/10.1016/j.actamat.2008.05.043.

Bober, D.B., Khalajhedayati, A., Kumar, M., Rupert, T.J., 2016. Grain boundary character distributions in nanocrystalline metals produced by different processing routes. Metall. Mater. Trans. A 47 (3), 1389–1403. http://dx.doi.org/10.1007/s11661-015-3274-9.

Borodin, E.N., Mayer, A.E., 2017. Influence of structure of grain boundaries and size distribution of grains on the yield strength at quasistatic and dynamical loading. Mater. Res. Express 4 (8), 085040. http://dx.doi.org/10.1088/2053-1591/aa8514.

Bouaziz, O., Estrin, Y., Bréchet, Y., Embury, J., 2010. Critical grain size for dislocation storage and consequences for strain hardening of nanocrystalline materials. Scr. Mater. 63 (5), 477–479. http://dx.doi.org/10.1016/j.scriptamat.2010.05.006.

Brink, T., Albe, K., 2018. From metallic glasses to nanocrystals: Molecular dynamics simulations on the crossover from glass-like to grain-boundary-mediated deformation behaviour. Acta Mater. 156, 205–214. http://dx.doi.org/10.1016/j.actamat.2018.06.036.

Bronkhorst, C.A., Kalidindi, S.R., Anand, L., 1992. Polycrystalline plasticity and the evolution of crystallographic texture in FCC metals. Philos. Trans.: Phys. Sci. Eng. 341 (1662), 443–477, URL http://www.jstor.org/stable/54154.

Carlton, C., Ferreira, P., 2007. What is behind the inverse hall–petch effect in nanocrystalline materials? Acta Mater. 55 (11), 3749–3756. http://dx.doi.org/10.1016/j.actamat.2007.02.021.

Challapalli Suryanarayana, 2012. Mechanical behavior of emerging materials. Mater. Today 15 (11), 486–498. http://dx.doi.org/10.1016/S1369-7021(12)70218-3.

Chen, Y., Li, H., Sun, G., Han, S., Lian, J., 2022. Unravelling the size-dependent mechanical properties of nanocrystalline face-centered-cubic metals: From the dislocation point of view. Adv. Eng. Mater. 24 (12), 2200601. http://dx.doi.org/10.1002/adem.202200601.

Chen, J., Lu, L., Lu, K., 2006. Hardness and strain rate sensitivity of nanocrystalline Cu. Scr. Mater. 54 (11), 1913–1918. http://dx.doi.org/10.1016/j.scriptamat.2006.02.022.

Chrominski, W., Lewandowska, M., 2018. Mechanisms of plastic deformation in ultrafine-grained aluminium – in-situ and ex-post studies. Mater. Sci. Eng. A 715, 320–331. http://dx.doi.org/10.1016/j.msea.2017.12.083.

Dalla Torre, F., Spätig, P., Schäublin, R., Victoria, M., 2005. Deformation behaviour and microstructure of nanocrystalline electrodeposited and high pressure torsioned nickel. Acta Mater. 53 (8), 2337–2349. http://dx.doi.org/10.1016/j.actamat.2005.01.041.

Dao, M., Lu, L., Asaro, R., De Hosson, J., Ma, E., 2007. Toward a quantitative understanding of mechanical behavior of nanocrystalline metals. Acta Mater. 55 (12), 4041–4065. http://dx.doi.org/10.1016/j.actamat.2007.01.038.

Estrin, Y., Mecking, H., 1984. A unified phenomenological description of work hardening and creep based on one-parameter models. Acta Metall. 32 (1), 57–70. http://dx.doi.org/10.1016/0001-6160(84)90202-5.

Farrokh, B., Khan, A.S., 2009. Grain size, strain rate, and temperature dependence of flow stress in ultra-fine grained and nanocrystalline Cu and Al: Synthesis, experiment, and constitutive modeling. Int. J. Plast. 25 (5), 715–732. http://dx.doi.org/10.1016/j.ijplas.2008.08.001.

Frazer, D., Bair, J.L., Homer, E.R., Hosemann, P., 2020. Cryogenic stress-driven grain growth observed via microcompression with in situ electron backscatter diffraction. JOM 72 (5), 2051–2056. http://dx.doi.org/10.1007/s11837-020-04075-x.

Fressengeas, C., Upadhyay, M.V., 2020. A continuum model for slip transfer at grain boundaries. Adv. Model. Simul. Eng. Sci. 7 (1), 12. http://dx.doi.org/10.1186/s40323-020-00145-6.

Frost, H.J., Ashby, M.F., 1982. Deformation-Mechanism Maps: The Plasticity and Creep of Metals and Ceramics. Pergamon Press.

Fu, H.-H., Benson, D.J., André Meyers, M., 2004. Computational description of nanocrystalline deformation based on crystal plasticity. Acta Mater. 52 (15), 4413–4425. http://dx.doi.org/10.1016/j.actamat.2004.05.036.

Gertsman, V., Birringer, R., 1994. On the room-temperature grain growth in nanocrystalline copper. Scr. Metall. Mater. 30 (5), 577–581. http://dx.doi.org/10.1016/0956-716X(94)90432-4.

Gifkins, R.C., 1976. Grain-boundary sliding and its accommodation during creep and superplasticity. Metall. Trans. A 7 (8), 1225–1232. http://dx.doi.org/10.1007/BF02656607.

Gu, Y., Cappola, J., Wang, J., Li, L., 2023. A hall-petch-like relationship linking nanoscale heterogeneity to yield stress of heterogeneous metallic glasses. Int. J. Plast. 170, 103759. http://dx.doi.org/10.1016/j.ijplas.2023.103759.

Gubicza, J., Pereira, P.H.R., Kapoor, G., Huang, Y., Vadlamani, S.S., Langdon, T.G., 2018. Annealing-induced hardening in ultrafine-grained Ni–Mo alloys. Adv. Eng. Mater. 20 (9), 1800184. http://dx.doi.org/10.1002/adem.201800184.

Guduru, R.K., Linga Murty, K., Youssef, K.M., Scattergood, R.O., Koch, C.C., 2007. Mechanical behavior of nanocrystalline copper. Mater. Sci. Eng. A 463 (1), 14–21. http://dx.doi.org/10.1016/j.msea.2006.07.165, TMS 2006, Mukherjee Symposium.

Gupta, S., Stangebye, S., Jungjohann, K., Boyce, B., Zhu, T., Kacher, J., Pierron, O.N., 2020. *In situ* TEM measurement of activation volume in ultrafine grained gold. Nanoscale 12, 7146–7158. http://dx.doi.org/10.1039/D0NR01874K.

Ha, S., Jang, J.-H., Kim, K., 2017. Finite element implementation of dislocation-density-based crystal plasticity model and its application to pure aluminum crystalline materials. Int. J. Mech. Sci. 120, 249–262. http://dx.doi.org/10.1016/j.ijmecsci.2016.11.011.

Hamid, M., Lyu, H., Schuessler, B.J., Wo, P.C., Zbib, H.M., 2017. Modeling and characterization of grain boundaries and slip transmission in dislocation density-based crystal plasticity. Crystals 7 (6), http://dx.doi.org/10.3390/cryst7060152.

Hao, Y., Tan, C., Yu, X., Chen, R., Nie, Z., Ren, Y., Yang, S., Li, Y., Wang, F., 2020. Effect of grain boundary misorientation angle on diffusion behavior in molybdenum-tungsten systems. J. Alloys Compd. 819, 152975. http://dx.doi.org/10.1016/j.jallcom.2019.152975.

Haouaoui, M., Karaman, I., Harwig, K.T., Maier, H.J., 2004. Microstructure evolution and mechanical behavior of bulk copper obtained by consolidation of micro- and nanopowders using equal-channel angular extrusion. Metall. Mater. Trans. A 35 (9), 2935–2949. http://dx.doi.org/10.1007/s11661-004-0241-2.

Hochhalter, J., Bomarito, G., Yeratapally, S., Leser, P., Ruggles, T., Warner, J., Leser, W., 2020. Non-deterministic calibration of crystal plasticity model parameters. In: Ghosh, S., Woodward, C., Przybyla, C. (Eds.), Integrated Computational Materials Engineering (ICME): Advancing Computational and Experimental Methods. Springer International Publishing, Cham, pp. 165–198. http://dx.doi.org/10.1007/978-3-030-40562-5_6.

Hollang, L., Hieckmann, E., Brunner, D., Holste, C., Skrotzki, W., 2006. Scaling effects in the plasticity of nickel. Mater. Sci. Eng. A 424 (1), 138–153. http://dx.doi.org/10.1016/j.msea.2006.03.002.

Husain, A., La, P., Hongzheng, Y., Jie, S., 2020. Molecular dynamics as a means to investigate grain size and strain rate effect on plastic deformation of 316 L nanocrystalline stainless-steel. Materials 13 (14), 3223. http://dx.doi.org/10.3390/ma13143223.

Jeong, H., Kim, W., 2023. Effects of grain size and Al addition on the activation volume and strain-rate sensitivity of CoCrFeMnNi high-entropy alloy. J. Mater. Sci. Technol. 143, 242–252. http://dx.doi.org/10.1016/j.jmst.2022.09.048.

Kalidindi, S., Bronkhorst, C., Anand, L., 1992. Crystallographic texture evolution in bulk deformation processing of FCC metals. J. Mech. Phys. Solids 40 (3), 537–569. http://dx.doi.org/10.1016/0022-5096(92)80003-9.

Kato, M., 2009. Thermally activated dislocation depinning at a grain boundary in nanocrystalline and ultrafine-grained materials. Mater. Sci. Eng. A 516 (1), 276–282. http://dx.doi.org/10.1016/j.msea.2009.03.035.

Kato, M., Fujii, T., Onaka, S., 2008. Dislocation bow-out model for yield stress of ultra-fine grained materials. Mater. Trans. 49 (6), 1278–1283. http://dx.doi.org/10.2320/matertrans.MRA2008012.

Khan, A.S., Farrokh, B., Takacs, L., 2008. Compressive properties of Cu with different grain sizes: sub-micron to nanometer realm. J. Mater. Sci. 43 (9), 3305–3313. http://dx.doi.org/10.1007/s10853-008-2508-2.

Khan, A.S., Liu, J., 2016. A deformation mechanism based crystal plasticity model of ultrafine-grained/nanocrystalline FCC polycrystals. Int. J. Plast. 86, 56–69. http://dx.doi.org/10.1016/j.ijplas.2016.08.001.

Koch, C., 2003. Optimization of strength and ductility in nanocrystalline and ultrafine grained metals. Scr. Mater. 49 (7), 657–662. http://dx.doi.org/10.1016/S1359-6462(03)00394-4, Viewpoint Set No. 31. Mechanical Properties of Fully Dense Nanocrystalline Metals.

Kocks, U.F., Argon, A.S., Ashby, M.F., 1975. Thermodynamics and Kinetics of Slip. Pergamon Press.

Kolonits, T., Jenei, P., Tóth, B.G., Czigány, Z., Gubicza, J., Péter, L., Bakonyi, I., 2015. Characterization of defect structure in electrodeposited nanocrystalline Ni films. J. Electrochem. Soc. 163 (3), http://dx.doi.org/10.1149/2.0911603jes.

Kumar, K., Suresh, S., Chisholm, M., Horton, J., Wang, P., 2003. Deformation of electrodeposited nanocrystalline nickel. Acta Mater. 51 (2), 387–405. http://dx.doi.org/10.1016/S1359-6454(02)00421-4.

Lee, E.H., 1969. Elastic-plastic deformation at finite strains. J. Appl. Mech. 36 (1), 1–6. http://dx.doi.org/10.1115/1.3564580.

Lee, M., Lim, H., Adams, B., Hirth, J., Wagoner, R., 2010. A dislocation density-based single crystal constitutive equation. Int. J. Plast. 26 (7), 925–938. http://dx.doi.org/10.1016/j.ijplas.2009.11.004.

Legland, D., 2023. matGeom. https://github.com/mattools/matGeom/releases/tag/v1.2.6.

Li, L., Anderson, P.M., Lee, M.-G., Bitzek, E., Derlet, P., Swygenhoven, H.V., 2009a. The stress–strain response of nanocrystalline metals: A quantized crystal plasticity approach. Acta Mater. 57 (3), 812–822. http://dx.doi.org/10.1016/j.actamat.2008.10.035.

Li, J.C.M., Feng, C.R., Rath, B.B., 2021. Emission of dislocations from grain boundaries and its role in nanomaterials. Crystals 11 (1), http://dx.doi.org/10.3390/cryst11010041.

Li, L., Lee, M.-G., Anderson, P.M., 2011. Critical strengths for slip events in nanocrystalline metals: Predictions of quantized crystal plasticity simulations. Metall. Mater. Trans. A 42 (13), 3875–3882. http://dx.doi.org/10.1007/s11661-010-0392-2.

Li, L., Ungár, T., Wang, Y., Morris, J., Tichy, G., Lendvai, J., Yang, Y., Ren, Y., Choo, H., Liaw, P., 2009b. Microstructure evolution during cold rolling in a nanocrystalline Ni–Fe alloy determined by synchrotron X-ray diffraction. Acta Mater. 57 (17), 4988–5000. http://dx.doi.org/10.1016/j.actamat.2009.07.002.
Lide, D., 2009. CRC Handbook of Chemistry and Physics, ninetieth ed. Taylor & Francis.
Liu, G., Xie, D., Wang, S., Misra, A., Wang, J., 2019. Mesoscale crystal plasticity modeling of nanoscale Al–Al_2Cu eutectic alloy. Int. J. Plast. 121, 134–152. http://dx.doi.org/10.1016/j.ijplas.2019.06.008.
Lohmiller, J., Grewer, M., Braun, C., Kobler, A., Kübel, C., Schüler, K., Honkimäki, V., Hahn, H., Kraft, O., Birringer, R., Gruber, P.A., 2014. Untangling dislocation and grain boundary mediated plasticity in nanocrystalline nickel. Acta Mater. 65, 295–307. http://dx.doi.org/10.1016/j.actamat.2013.10.071.
Lu, K., 2016. Stabilizing nanostructures in metals using grain and twin boundary architectures. Nat. Rev. Mater. 1 (5), 16019. http://dx.doi.org/10.1038/natrevmats.2016.19.
Malygin, G.A., 2007a. Analysis of the strain-rate sensitivity of flow stresses in nanocrystalline FCC and BCC metals. Phys. Solid State 49 (12), 2266–2273. http://dx.doi.org/10.1134/S1063783407120098.
Malygin, G.A., 2007b. Plasticity and strength of micro- and nanocrystalline materials. Phys. Solid State 49 (6), 1013–1033. http://dx.doi.org/10.1134/S1063783407060017.
McKenzie, D., 1979. Finite deformation during fluid flow. Geophys. J. R. Astron. Soc. 58 (3), 689–715. http://dx.doi.org/10.1111/j.1365-246X.1979.tb04803.x.
Mecking, H., Kocks, U., 1981. Kinetics of flow and strain-hardening. Acta Metall. 29 (11), 1865–1875. http://dx.doi.org/10.1016/0001-6160(81)90112-7.
Meyers, M., Mishra, A., Benson, D., 2006. Mechanical properties of nanocrystalline materials. Prog. Mater. Sci. 51 (4), 427–556. http://dx.doi.org/10.1016/j.pmatsci.2005.08.003.
Nes, E., Holmedal, B., Evangelista, E., Marthinsen, K., 2005. Modelling grain boundary strengthening in ultra-fine grained aluminum alloys. Mater. Sci. Eng. A 410–411, 178–182. http://dx.doi.org/10.1016/j.msea.2005.08.121.
Nguyen, N., Waas, A.M., 2016. Nonlinear, finite deformation, finite element analysis. Z. Angew. Math. Phys. 67 (3), 35. http://dx.doi.org/10.1007/s00033-016-0623-5.
Ovid'ko, I.A., Sheinerman, A.G., 2003. Grain-boundary dislocations and enhanced diffusion in nanocrystalline bulk materials and films. Phil. Mag. 83 (13), 1551–1563. http://dx.doi.org/10.1080/1478643031000088674.
Pan, Z., Rupert, T.J., 2014. Damage nucleation from repeated dislocation absorption at a grain boundary. Comput. Mater. Sci. 93, 206–209. http://dx.doi.org/10.1016/j.commatsci.2014.07.008.
Quey, R., Dawson, P., Barbe, F., 2011. Large-scale 3D random polycrystals for the finite element method: Generation, meshing and remeshing. Comput. Methods Appl. Mech. Engrg. 200 (17), 1729–1745. http://dx.doi.org/10.1016/j.cma.2011.01.002.
Simo, J.C., Hughes, T.J.R., 1998. Computational Inelasticity. Springer-Verlag.
Smith, M., 2009. ABAQUS/Standard User's Manual, Version 6.9. Dassault Systèmes Simulia Corp, United States.
Sobie, C., Capolungo, L., McDowell, D.L., Martinez, E., 2017. Modal analysis of dislocation vibration and reaction attempt frequency. Acta Mater. 134, 203–210. http://dx.doi.org/10.1016/j.actamat.2017.02.005.
Surholt, T., Herzig, C., 1997. Grain boundary self-diffusion in Cu polycrystals of different purity. Acta Mater. 45 (9), 3817–3823. http://dx.doi.org/10.1016/S1359-6454(97)00037-2.
Taupin, V., Capolungo, L., Fressengeas, C., Upadhyay, M., Beausir, B., 2015. A mesoscopic theory of dislocation and disclination fields for grain boundary-mediated crystal plasticity. Int. J. Solids Struct. 71, 277–290. http://dx.doi.org/10.1016/j.ijsolstr.2015.06.031.
Taylor, G.I., 1938. Plastic strain in metals. J. Inst. Metals 62, 307–324.
Turlo, V., Rupert, T.J., 2018. Grain boundary complexions and the strength of nanocrystalline metals: Dislocation emission and propagation. Acta Mater. 151, 100–111. http://dx.doi.org/10.1016/j.actamat.2018.03.055.
Vetterick, G.A., Gruber, J., Suri, P.K., Baldwin, J.K., Kirk, M.A., Baldo, P., Wang, Y.Q., Misra, A., Tucker, G.J., Taheri, M.L., 2017. Achieving radiation tolerance through non-equilibrium grain boundary structures. Sci. Rep. 7 (1), 12275. http://dx.doi.org/10.1038/s41598-017-12407-2.
Wang, Y., Hamza, A., Ma, E., 2006. Temperature-dependent strain rate sensitivity and activation volume of nanocrystalline Ni. Acta Mater. 54 (10), 2715–2726. http://dx.doi.org/10.1016/j.actamat.2006.02.013.
Wang, Y.M., Ma, E., 2004. On the origin of ultrahigh cryogenic strength of nanocrystalline metals. Appl. Phys. Lett. 85 (14), 2750–2752. http://dx.doi.org/10.1063/1.1799238.
Wang, Y., Ma, E., Valiev, R., Zhu, Y., 2004. Tough nanostructured metals at cryogenic temperatures. Adv. Mater. 16 (4), 328–331. http://dx.doi.org/10.1002/adma.200305679.
Wang, J., Zhou, Q., Shao, S., Misra, A., 2017. Strength and plasticity of nanolaminated materials. Mater. Res. Lett. 5 (1), 1–19. http://dx.doi.org/10.1080/21663831.2016.1225321.
Wei, B., Wu, W., Nastasi, M., Li, L., Wang, J., 2022. Plastic flow behaviors of high-strength dual-phase Ni-SiOC nanocomposites. Int. J. Plast. 158, 103431. http://dx.doi.org/10.1016/j.ijplas.2022.103431.
Wei, B., Wu, W., Xie, D., Nastasi, M., Wang, J., 2021. Strength, plasticity, thermal stability and strain rate sensitivity of nanograined nickel with amorphous ceramic grain boundaries. Acta Mater. 212, 116918. http://dx.doi.org/10.1016/j.actamat.2021.116918.
Witkin, D., Han, B.Q., Lavernia, E.J., 2005. Mechanical behavior of ultrafine-grained cryomilled Al 5083 at elevated temperature. J. Mater. Eng. Perform. 14 (4), 519–527. http://dx.doi.org/10.1361/105994905X56232.
Wu, X.-L., Ma, E., 2006. Dislocations in nanocrystalline grains. Appl. Phys. Lett. 88 (23), 231911. http://dx.doi.org/10.1063/1.2210295.
Yamakov, V., Wolf, D., Salazar, M., Phillpot, S., Gleiter, H., 2001. Length-scale effects in the nucleation of extended dislocations in nanocrystalline Al by molecular-dynamics simulation. Acta Mater. 49 (14), 2713–2722. http://dx.doi.org/10.1016/S1359-6454(01)00167-7.
Youssef, K.M., Scattergood, R.O., Murty, K.L., Horton, J.A., Koch, C.C., 2005. Ultrahigh strength and high ductility of bulk nanocrystalline copper. Appl. Phys. Lett. 87 (9), 091904. http://dx.doi.org/10.1063/1.2034122.
Yuan, R., Beyerlein, I.J., Zhou, C., 2015. Emergence of grain-size effects in nanocrystalline metals from statistical activation of discrete dislocation sources. Acta Mater. 90, 169–181. http://dx.doi.org/10.1016/j.actamat.2015.02.035.
Yujie Wei, Cheng Su, Lallit Anand, 2006. A computational study of the mechanical behavior of nanocrystalline fcc metals. Acta Mater. 54 (12), 3177–3190. http://dx.doi.org/10.1016/j.actamat.2006.03.007.
Zhang, Y., Gigax, J.G., Nizolek, T.J., Carpenter, J.S., Schneider, M.M., Li, N., Capolungo, L., McCabe, R.J., 2022. Tensile and failure behaviors of Cu/Nb nanolaminates: the effects of loading direction, layer thickness, and annealing. Acta Mater. 240, 118346. http://dx.doi.org/10.1016/j.actamat.2022.118346.
Zhang, K., Weertman, J.R., Eastman, J.A., 2004. The influence of time, temperature, and grain size on indentation creep in high-purity nanocrystalline and ultrafine grain copper. Appl. Phys. Lett. 85 (22), 5197–5199. http://dx.doi.org/10.1063/1.1828213.
Zhao, J., Kan, Q., Zhou, L., Kang, G., Fan, H., Zhang, X., 2019. Deformation mechanisms based constitutive modelling and strength-ductility mapping of gradient nano-grained materials. Mater. Sci. Eng. A 742, 400–408. http://dx.doi.org/10.1016/j.msea.2018.10.096.
Zhilyaev, A.P., Langdon, T.G., 2008. Using high-pressure torsion for metal processing: Fundamentals and applications. Prog. Mater. Sci. 53 (6), 893–979. http://dx.doi.org/10.1016/j.pmatsci.2008.03.002.
Zhu, B., Asaro, R., Krysl, P., Bailey, R., 2005. Transition of deformation mechanisms and its connection to grain size distribution in nanocrystalline metals. Acta Mater. 53 (18), 4825–4838. http://dx.doi.org/10.1016/j.actamat.2005.06.033.
Zhu, B., Asaro, R., Krysl, P., Zhang, K., Weertman, J., 2006. Effects of grain size distribution on the mechanical response of nanocrystalline metals: Part II. Acta Mater. 54 (12), 3307–3320. http://dx.doi.org/10.1016/j.actamat.2006.03.022.
Zhu, Y.T., Liao, X., 2004. Retaining ductility. Nature Mater. 3 (6), 351–352. http://dx.doi.org/10.1038/nmat1141.